A Single-Reciprocating-Piston Two-Phase Thermofluidic Prime-Mover

Aly I. Taleb[a], Michael A. G. Timmer[a], Mohamed Y. El-Shazly[a], Aleksandr Samoilov[b,c], Valeriy A. Kirillov[b,c,d], Christos N. Markides[a,*]

[a] *Clean Energy Processes (CEP) Laboratory, Department of Chemical Engineering, Imperial College London, South Kensington Campus, London SW7 2AZ, U.K.*
[b] *Boreskov Institute of Catalysis (BIC), pr. Lavrentieva 5, Novosibirsk, Russia, 630090*
[c] *Limited Liability Company "UNICAT", pr. Lavrentieva 5, Novosibirsk, Russia, 630090*
[d] *Novosibirsk State University, Pirogova St. 2, Novosibirsk, Russia, 630090*

Abstract

We explore theoretically a thermodynamic heat-engine concept that has the potential of attaining a high efficiency and power density relative to competing solutions, while having a simple construction with few moving parts and dynamic seals, allowing low capital and operating costs, and long lifetimes. Specifically, an unsteady heat-engine device within which a working fluid undergoes a power cycle featuring phase-change, termed the 'Evaporative Reciprocating-Piston Engine' (ERPE), is considered as a potential prime mover for use in combined heat and power (CHP) applications. Based on thermal/fluid-electrical analogies, a theoretical ERPE device is conceptualized initially in the electrical-analogy domain as a linearized, closed-loop active electronic circuit model. The circuit-model representation is designed to potentially exhibit high efficiencies compared to similar, existing two-phase unsteady heat engines. From the simplified circuit model in the electrical domain, and using the thermal/fluid-electrical analogies, one possible configuration of a corresponding physical ERPE device is derived, based on an early prototype of a device currently under development that exhibits some similarities with the ERPE, and used as a physical manifestation of the proposed concept. The corresponding physical ERPE device relies on the alternating phase change of a suitable working-fluid (here, water) to drive a reciprocating displacement of a single vertical piston and to produce sustained oscillations of thermodynamic properties within an enclosed space. Four performance indicators are considered: the operational frequency, the power output, the exergy efficiency, and the heat input/temperature difference imposed externally on the device's heat exchangers that is necessary to sustain oscillations. The effects of liquid inertia, viscous drag, hydrostatic pressure, vapour compressibility and two-phase heat transfer in the various engine components/compartments are examined, via changes to thermodynamic/thermophysical/transport properties and also geometrical features of the ERPE. It is found that for high efficiency and power output: (1) the vapour dead-spaces must be minimized; (2) the length of the tube that connects the displacer and working cylinders must be of significant length; and, (3) the heat-exchanger blocks must have a low thermal resistance and high heat capacity. The methodological approach implemented in this study can be used to guide the proposal, early-stage design and verification of these complex unsteady thermodynamic systems, while offering important suggestions for improved performance and system optimization.

*Corresponding author, Tel.: +44 (0)20 759 41601
Email address: c.markides@imperial.ac.uk (Christos N. Markides)
URL: www.imperial.ac.uk/cep (Christos N. Markides)

Keywords: heat engine; heat converter; thermofluidic oscillator; unsteady; two-phase; electrical analogy

---

Highlights

- A new two-phase unsteady thermofluidic oscillator engine concept is proposed
- A physical device with a vertical reciprocating-piston is derived from an electrical model
- Realistic operational frequencies and necessary heat inputs are estimated
- Small dead-spaces and a long connecting tube allow improved performance

1. Introduction

1.1. Motivation

A variety of drivers have been promoting an enhanced interest in the decentralized combined production or co-generation of heat and power (CHP). These drivers include a desire for the secure supply of sustainable primary energy, health and environmental concerns arising from the emission of combustion gases to the atmosphere, the increasing penetration of intermittent renewables into the electricity grid and the aspiration to provide heating and/or power to remote areas with no or intermittent energy supplies [1, 2]. The EU has been addressing the issue of energy security, and one of the priorities has been to improve energy efficiency through the creation of a decentralized network of low-power cogeneration plants [3]. The decentralized framework arises from an incentive to minimize transmission and distribution losses on the one hand; and on the other, it allows a greater flexibility and variation of the delivered power depending on the local demand. Conventional external-combustion prime-mover technologies, such as Rankine/steam and Stirling-cycle engines, can be relatively complex, operationally inflexible (e.g., at part loads) and expensive at small scales and low power outputs, which is why they have been largely displaced by internal combustion engines in relevant applications. Beyond issues with vibration and noise, however, conventional internal combustion engines cannot directly utilize external heat sources and are designed for the direct consumption of fossil fuels. In addition, they have relatively high maintenance requirements owing to complex mechanical arrangements and moving seals. This motivates the proposal and development of a prime mover with the following desirable characteristics: (1) efficient power generation at small scales and low power outputs between 1 and 100 kW; and (2) compatibility with a diverse variety of heat sources such as waste heat, solar, geothermal, fossil fuels, etc. Relevant heat engine technologies (e.g., organic Rankine cycle, Kalina or Stirling cycles) with power outputs below 100 kW have investment costs in the order of 2−4 £/W_{el} [1, 2, 4–6] whereby the costs per unit power output tend to increase at very low power outputs. Therefore, at these low power ranges, the prime mover must be extremely cost-efficient for the CHP system to be economically viable.

Thermofluidic oscillator (TFO) engines (or converters) promise to be a particularly cost-efficient solution to this challenge. TFOs are a class of unsteady heat-engine within which persistent periodic thermodynamic oscillations are induced from static (steady) external thermal conditions [7]. In practice, a TFO is a network of interconnected tubes and chambers that features no or few mechanical moving-parts and seals. Thanks to its simple construction and operation, a TFO typically has low capital costs and low maintenance requirements. The working fluid is subjected to time-varying heat transfer by alternating thermal contact with a pair of hot and cold heat exchangers. This alternating heat-exchange process induces thermodynamic property oscillations of pressure, volume and temperature, giving rise to an oscillatory fluid motion. Consequently, an unsteady thermodynamic cycle is sustained that is capable of converting thermal energy to hydraulic or pumping work with the use of a (liquid or solid) piston [8]. A variety of heat sources and sinks can be used to provide and extract heat to and from the heat exchangers. TFOs can take the form of single-/gas-phase

systems such as thermoacoustic [9–14] and Fluidyne engines [15–18], or two-/vapour-phase systems such as the 'Non-Inertive-Feedback Thermouidic Engine' (NIFTE) [7, 19–25].

1.2. Objectives

In this paper we conceptualize and investigate theoretically a two-phase TFO that we term the 'Evaporative Reciprocating-Piston Engine' (ERPE). In two-phase TFOs, such as the ERPE and the aforementioned NIFTE, periodic heat addition to and rejection from a working fluid lead to alternating phase-change (evaporation and condensation), and consequent pressure and volumetric displacement variations within the device. Phase change allows TFOs to operate across low temperature differences between the heat source and sink, and facilitates small heat exchanger surfaces per unit heat transferred. During the heat addition (evaporation) phase, the mass of vapour inside the device increases leading to an increase in the pressure of the vapour volume. This, in turn, leads to a positive displacement of a liquid piston into a hydraulic load. Conversely, during the heat rejection phase, condensation in the vapour space results in a pressure reduction which produces a suction stroke. These alternating pressure and volume oscillations produce hydraulic work that can be harnessed to drive a generator at the load.

The goal of this research is to develop a theoretical ERPE concept which has the potential to exhibit a higher efficiency and frequency compared to competing TFOs. The approach follows the methods employed earlier by Backhaus and Swift [12, 13], Ceperley [26], Smith [7, 27], Markides et al. [19, 23, 24] and Solanki et al. [20–22] according to which analogies are drawn between thermofluid processes in the device and passive electrical components. This method was validated successfully in the context of two-phase TFOs against experimental data obtained from a NIFTE prototype [20–22], and has proven to be useful in promoting an improved understanding of the operation and performance, and also the early-stage design and optimization [25], of this technology. Initially and based on the electrical analogies, the ERPE concept is defined in the analogy domain as an electronic circuit model representation of an engine of which a physical description is still undefined. Subsequently and based on an existing device that bares some degree of similarity to the ERPE in the electrical analogy domain, approximate values of important electrical parameters and a possible physical configuration are taken as indications of the design space within which an ERPE may be realised. Consequently, a physical design of a possible ERPE oscillator is derived from the electronic circuit and used in the remainder of the study. This approach is a reversal of the conventional approach whereby an existing physical representation of an engine (e.g., an actual prototype or an existing design) is modelled to understand its behaviour and predict its performance. By reversing this process and starting in the electrical analogy domain, we can from the very beginning design an engine which fulfils specific desired criteria—in our case, a comparably high efficiency and power density.

To define the values of the components in the ERPE circuit and thereby develop a physical ERPE device, the geometric parameters and thermodynamic/thermophysical fluid properties relating to a TFO engine prototype currently being tested at the Boreskov Institute of Catalysis (BIC) are adopted to the new concept [28]. This prototype, which is an evolution of one originally developed by Encontech B.V. (www.encontech.nl)

[29], has been selected as it bears several similarities to one of the possible physical representations of the ERPE, as proposed here. Additionally, we use experimental data of pressure variations provided by BIC of their prototype as indicative values to assess if the present model predictions are realistic. Two different sub-models of the heat transfer processes at the heat exchangers of the device are compared. The first model assumes a linear temperature profile (LTP) along the height of the hot and cold heat exchanger surfaces. The second model accounts for the dynamic ability of the heat exchanger walls (DHX) to store and release heat periodically by considering explicitly the unsteady energy balance that describes the heat addition (or rejection) from the external heat source (or sink) [22]. Subsequently, a parametric study is performed in which different component characteristics are varied to examine their influence on the engine's performance indicators, i.e., the operational/oscillation frequency, power output, efficiency, and necessary heat input for sustained operation/oscillation.

2. ERPE Configuration and Operation

Figures 7(a) and (b) show two electronic circuit representations of the ERPE, where: (a) is an engine with no load, and (b) includes a load at the far right-hand side. The circuits have been defined to potentially produce high exergetic efficiencies and frequencies compared to other TFOs (see Section 4.2). They consist of a voltage/potential source and a number of resistances (R), inductances (L) and capacitances (C). A certain combination of electrical elements can represent a specific component of a TFO to a first-order approximation. For instance, a resistance, inductance and capacitance in series can describe a liquid column, while a capacitance connected to ground can describe a gas spring (see Section 3). The values of the electrical elements are functions of geometric and thermodynamic properties of the physical representation of the engine which have yet to be defined. A possible physical description of the ERPE is shown in Fig. 8 which has been derived to be as close as possible to the BIC prototype [28]. This physical representation will be used for the whole scope of the study. The geometry and thermodynamic properties of the BIC prototype will be imposed on the physical representation of the ERPE where possible to provide realistic values for the electrical elements. In the interest of comprehension, the electronic circuit model is described in the following sections as being derived from the physical representation, when in actuality, the physical representation of the engine is derived from the circuit. Using the physical representation as a starting point is the more conventional approach, and it is therefore the easier approach for the reader to understand.

The volume at the top of the displacer cylinder in Fig. 8 contains working fluid in the vapour phase, which behaves as a gas spring. This section is surrounded by the hot heat exchanger (HHX) which adds heat and evaporates the working fluid—in this case water. Below the HHX is the cold heat exchanger (CHX) section, which extracts heat from the working fluid and condenses it. Connected to the displacer piston is a mechanical spring which moves freely with the piston. The working cylinder, on the left-hand side, consists of a gas spring (argon gas) entrapped by a liquid column. The two cylinders are connected by a tube equipped with an adjustable valve through which the engine's power output can be assessed. When

the valve is completely open, the engine is considered to run without a load.

Since the ERPE is an oscillator, understanding the processes undergone in one reciprocating cycle fully explains its operation. Assuming a cycle to start at the top dead center (TDC) of the solid piston, the liquid-vapour interface is in contact with the HHX such that heat is added to the working fluid. The working fluid evaporates, generating vapour and leading to a pressure increase in the vapour gas spring. This pressure drives a downward acceleration of the liquid level and of the displacer piston which overshoot their equilibrium positions (halfway between the two heat exchangers) due to their inertia. The vapour-liquid interface and the displacer piston always move in the same direction albeit not necessarily at the same speeds. The displacer piston is assumed to be always completely immersed in water. Water flows through the load in the connection tube—thereby dissipating work—into the working cylinder elevating its water level and compressing the argon gas spring. A hydrostatic pressure difference is created between the water levels of the two cylinders. Gradually, the CHX surfaces are exposed to the hot vapour, which begins to condense. The condensation process leads to a decrease in pressure in the vapour region. The increasing hydrostatic pressure difference between the displacer and working cylinders, the increasing compression of the mechanical and gas springs and the decreasing pressure in the vapour region exert restoring or suction forces on the piston and the water column. However, for a limited time, the piston and water column continue their downward displacement due to their momentum, while gradually decelerating.

As the displacer piston reaches bottom dead centre (BDC), the restoring hydrostatic, spring and gas compressibility forces gradually lead to a reversal of the piston and flow direction. The water level and the displacer piston accelerate upwards and overshoot their equilibrium positions due to their inertia. Once again, the hydrostatic pressure difference and the gas and mechanical springs create restoring forces; this time, in the opposite direction, thus gradually decelerating the rising piston and water level until they reach TDC where their movement is reversed. In this manner, a full cycle is completed.

3. Model Development

The development of the ERPE electronic circuit model will be described in detail below. It will be presented as a derivation from a physical representation of the ERPE in order to make it easier for the reader. In this study, however, the starting point for the conceptual development of the ERPE was the electrical-analogy model that was transformed into a physical device at later stage, as mentioned in the previous section.

If a physical engine representation exists, a set of linearized, spatially lumped sub-models can be derived for every component of the engine, each of which describes the dominant thermal or fluid process in a particular component with an ordinary differential equation (ODE). Using electrical analogies, the resulting ODEs can be represented by a combination of passive electrical components such as resistors, inductors and capacitors. These are then interconnected to form an electronic circuit representation of the entire device.

Specifically, thermal resistance, fluid drag and viscosity are accounted for by introducing resistors R, gravity and gas compressibility are described by capacitors C, and fluid/piston inertia by inductors L. The

voltage across an element is equivalent to a pressure P at the corresponding engine location, whereas the current is equivalent to the resulting volumetric flow-rate U through it. At the heat exchangers, the voltage corresponds to a temperature and the current corresponds to an entropy flow-rate; both are converted into an equivalent pressure and volumetric flow-rate as explained in previous work [19–24]. Applying Gauss's, Faraday's and Ohm's laws in the electrical analogy leads to the following three fundamental equations between pressure P and flow-rate U which, with the help of the principle of superposition, can account for more than one process or effect within a particular component:

$$\frac{\mathrm{d}(\Delta P)}{\mathrm{d}t} = \frac{1}{C}U\,, \qquad \Delta P = L\frac{\mathrm{d}U}{\mathrm{d}t}\,, \qquad \Delta P = RU\,, \tag{1}$$

or in the Laplace domain:

$$\Delta P = \frac{1}{sC}U\,, \qquad \Delta P = sLU\,, \qquad \Delta P = RU\,, \tag{2}$$

where $s = \sigma + i\omega$ is the Laplace variable.

The main components of the engine in which dominant processes occur that must be captured in the model are highlighted in Fig. 8, and these include the heat exchangers ('hx'), the vapour region in the displacer cylinder ('v'), the solid displacer piston ('p') and the leakage flow around it ('l'), the slide bearing in the displacer cylinder ('b'), the liquid column in the displacer cylinder ('d') and in the working cylinder ('w'), in the load-free engine), the gas spring ('g'), in the load-free engine), the load ('lo') and the connection tube ('c'). These components and the associated processes are discussed in detail in the following sections.

Because the engine is a periodically oscillating device, all thermodynamic, thermal and fluid-mechanical quantities can be expressed as the sum of time-averaged and fluctuating components. For example, a pressure can be expressed as $P(t) = \overline{P} + P'(t)$ and a volumetric flow-rate as $U(t) = \overline{U} + U'(t)$, where the overbar denotes time-averaged quantities and the prime denotes fluctuating values. The time-mean values are also referred to as equilibrium values. Only the fluctuating components are considered in the present linear modelling approach. Similarly to earlier work on the NIFTE, it is assumed that the time-varying quantities are small fluctuations around their respective time-mean values, e.g., $P' \ll \overline{P}$. Therefore, for simplicity, the prime symbol will be henceforth dropped, and any variables (pressure, temperature, flow-rate, etc.) mentioned will refer to the fluctuating, time-varying components of these quantities.

The definitions and nominal values of the electrical components are listed in Table 1. Their derivations can be found in Refs. [19–22]. To calculate the nominal values, the geometric dimensions of the BIC prototype are adopted along with relevant properties of the presently selected working fluid, water.

3.1. Phase-change/thermal domain and heat exchangers

The liquid columns in the cylinders or tubes can be described with a resistance representing viscous drag, an inductance for the column's inertia and a capacitance for the hydrostatic pressure difference (not for the

connection tube as it is horizontal) which can be deduced from a force balance on the liquid column:

$$R = \frac{128\mu l_0}{\pi d^4}\,, \qquad L = \frac{\rho_{\mathrm{wf}} l_0}{A}\,, \qquad C = \frac{A}{\rho_{\mathrm{wf}} g}\,, \tag{3}$$

where μ and ρ_{wf} are the dynamic viscosity and density of the liquid working fluid, l_0 is the equilibrium length of the liquid column, d is the diameter of the cross-section, A is the cross-section area and g is the gravitational acceleration. The Reynolds and Womersley numbers of the flow are sufficiently low to assume quasi-steady, viscous laminar and fully developed flow. Flow losses at sudden contractions and expansions are neglected. Gas springs are considered adiabatic and reversible (isentropic), and are modelled by capacitances that can be derived by linearizing the isentropic perfect-gas relations. The resulting capacitance is:

$$C = \frac{V_0}{\gamma P_0}\,. \tag{4}$$

Here, V_0 and P_0 are the gas spring equilibrium volume and pressure, and γ is the ratio of specific heats of the gas or vapour. The heat exchanger components (see Figure 8) stem from a heat balance at the heat exchangers, the change in entropy due to phase change and the Clausius-Clapeyron relation. This leads to a resistance and capacitance (in the DHX model; see Section 3.6 and Refs. [21, 22]) in series:

$$R_{\mathrm{th}} = \frac{\rho_{\mathrm{v},0} T_0 \Delta s_{\mathrm{fg}}}{h A_{\mathrm{s}} (\mathrm{d}T/\mathrm{d}P)_{\mathrm{sat}}}\,, \qquad C_{\mathrm{hx}} = \frac{m_{\mathrm{hx}} c_{\mathrm{hx}} (\mathrm{d}T/\mathrm{d}P)_{\mathrm{sat}}}{\rho_{\mathrm{v},0} T_0 \Delta s_{\mathrm{fg}}}\,, \tag{5}$$

where $\rho_{\mathrm{v},0}$ is the density of the vapour at equilibrium state, T_0 is the equilibrium temperature, Δs_{fg} is the entropy of vaporization, h is the heat transfer coefficient, A_{s} is the active surface area over which phase change heat transfer occurs, $(\mathrm{d}T/\mathrm{d}P)_{\mathrm{sat}}$ is the change of saturation temperature with pressure in the two-phase region, m_{hx} is the mass of a fixed part of the heat exchanger wall that participates in the heat transfer process and c_{hx} is the heat capacity of the heat exchanger walls. The definitions and nominal values of all electrical components are listed in Table 1. Their derivation can be found in Refs. [19–22].

3.2. Piston and leakage

The piston can be considered as comprising two parts. In the lower part, the piston is guided by the slide bearing and the flow is diverted and flows through two small channels (subscript 'b'). In the upper part, the piston moves freely and the liquid flows around it. For this upper part, a force balance on the solid piston (subscript 'p') and a linearized, one-dimensional Navier-Stokes equation for the leakage flow (subscript 'l') are applied, and coupling effects between the two motions are taken into account. This leads to a relation between the flow-rate of the liquid U_{l}, the (equivalent) flow-rate of the piston U_{p} and the pressure difference across the piston, based on which an impedance for the solid piston motion (Z_{p}) and for the liquid leakage flow (Z_{l}) are defined. Due to the coupling of the liquid flow and solid piston motion, the components relating to the flow are functions of parameters related to the piston, and vice versa. For example, the capacitance of the leakage flow C_{l} depends on the mechanical spring constant k_{ms}. It can be shown (see Appendix A) that

Table 1: Electrical analogies for the ERPE model. RLC relations and their respective nominal values at a mean pressure of 11.8 bar.

	Thermal-fluid effect	Parameter expression	Nominal Value
Resistances [kg/m^{4}s]	Thermal resistance	$R_{\mathrm{th}} = {\rho_{\mathrm{v},0}\Delta s_{\mathrm{fg}}T_0}/{hA_s(\mathrm{d}T/\mathrm{d}P)_{\mathrm{sat}}}$	2.08×10^{11}
	Displacer cylinder flow resistance	$R_{\mathrm{d}} = {128\mu}/{\pi}\left({l_{\mathrm{d,a}}}/{d_{\mathrm{d,a}}^4} + {l_{\mathrm{d,b}}}/{d_{\mathrm{d,b}}^4}\right)$	8.36×10^2
	Working cylinder flow resistance	$R_{\mathrm{w}} = {128\mu l_{\mathrm{w}}}/{\pi d_{\mathrm{w}}^4}$	6.08×10^3
	Connection tube flow resistance	$R_{\mathrm{c}} = {128\mu l_{\mathrm{c}}}/{\pi d_{\mathrm{c}}^4}$	1.11×10^6
	Solid piston resistance	$R_{\mathrm{p}} = {64h_{\mathrm{p}}\mu}/{\pi d_{\mathrm{p}}^2 c_1}$	1.23×10^5
	1st leakage flow resistance	$R_{\mathrm{l},1} = {128c_2h_{\mathrm{p}}\mu}/{\pi c_1 c_3}$	6.29×10^7
	2nd leakage flow resistance	$R_{\mathrm{l},2} = {128c_2h_{\mathrm{p}}\mu}/{\pi c_1(c_1 - 2c_2{d_{\mathrm{p}}}^2)}$	1.37×10^6
	Slide bearing piston resistance	$R_{\mathrm{b,p}} = {16\mu l_{\mathrm{b}}}/{\pi^2\delta d_{\mathrm{p}}^3}$	4.49×10^4
	Slide bearing flow resistance	$R_{\mathrm{b,l}} = {128\mu l_{\mathrm{b}}}/{\pi d_{\mathrm{b,l}}^4}$	2.44×10^6
Inductances [kg/m^4]	Displacer cylinder flow inertia	$L_{\mathrm{d}} = \rho_{\mathrm{wf}} l_{\mathrm{d,a}}\left({2}/{A_{\mathrm{d,a}}} - {Z_{\mathrm{pl}}}/{A_{\mathrm{p}}Z_{\mathrm{p}}} - {Z_{\mathrm{p}}}/{A_{\mathrm{l}}Z_{\mathrm{l}}}\right) + +\rho_{\mathrm{wf}} l_{\mathrm{d,b}}\left({Z_{\mathrm{pl}}}/{A_{\mathrm{p}}Z_{\mathrm{p}}} + {Z_{\mathrm{pl}}}/{A_{\mathrm{l}}Z_{\mathrm{l}}} - {1}/{A_{\mathrm{d,b}}}\right)$	1.12×10^6
	Working cylinder flow inertia	$L_{\mathrm{w}} = {4\rho_{\mathrm{wf}} l_{\mathrm{w}}}/{\pi d_{\mathrm{w}}^2}$	3.35×10^5
	Connection tube flow intertia	$L_{\mathrm{c}} = {4\rho_{\mathrm{wf}} l_{\mathrm{c}}}/{\pi d_{\mathrm{c}}^2}$	3.18×10^8
	Leakage flow inertia	$L_{\mathrm{l}} = {64c_2^2 m_{\mathrm{p}}}/{\pi^2 c_1(c_1 - 2c_2 d_{\mathrm{p}}^2)}$	7.11×10^7
	Piston inertia	$L_{\mathrm{p}} = {32c_2 m_{\mathrm{p}}}/{\pi^2 {d_{\mathrm{p}}}^2 c_1}$	7.44×10^6
	Slide bearing piston inertia	$L_{\mathrm{b,p}} = {4\rho_{\mathrm{ss}} l_{\mathrm{b}}}/{\pi {d_{\mathrm{p}}}^2}$	2.44×10^6
	Slide bearing flow inertia	$L_{\mathrm{b,l}} = {4\rho l_{\mathrm{sb}}}/{\pi d_{\mathrm{b,l}}^2}$	3.17×10^7
Capacitances [m^{4}s^2/kg]	Vapour gas spring capacitance	$C_{\mathrm{v}} = {V_{\mathrm{v}}}/{\gamma_{\mathrm{v}} P_{\mathrm{v,eq}}}$	2.07×10^{-11}
	Displacer hydrostatic capacitance	$C_{\mathrm{d}} = {\pi d_{\mathrm{d}}^2}/{4\rho_{\mathrm{wf}} g}$	2.60×10^{-8}
	Working hydrostatic capacitance	$C_{\mathrm{w}} = {\pi d_{\mathrm{w}}^2}/{4\rho_{\mathrm{wf}} g}$	7.31×10^{-8}
	Argon gas spring capacitance	$C_{\mathrm{g}} = {V_{\mathrm{g}}}/{\gamma_{\mathrm{g}} P_{\mathrm{g,eq}}}$	1.41×10^{-12}
	Piston capacitance	$C_{\mathrm{p}} = {\pi^2 d_{\mathrm{p}}^2 c_1}/{32k_{\mathrm{ms}}c_2}$	3.62×10^{-11}
	Leakage capacitance	$C_{\mathrm{l}} = {\pi^2 c_1(c_1 - c_2 d_{\mathrm{p}}^2)}/{64c_2^2 k_{\mathrm{ms}}}$	1.32×10^{-7}
	Heat exchanger capacitance	$C_{\mathrm{hx}} = {m_{\mathrm{hx}} c_{\mathrm{hx}}(\mathrm{d}T/\mathrm{d}P)_{\mathrm{sat}}}/{\rho_{\mathrm{v},0}\Delta s_{\mathrm{fg}} T_0}$	1.10×10^{-12}

these impedances can be manipulated such that the circuit consisting of the components presented in Fig. 9 and Eq. 6 are derived. A physical and intuitive understanding of these components in isolation is difficult. For example, the division of U_{l} in Fig. 9 into two parallel branches, $U_{\mathrm{l},1}$ and $U_{\mathrm{l},2}$, cannot be understood physically, as there is no actual separation of the flow in this part of the engine. These interconnections and components are a result of algebraic manipulations of the coupled Navier-Stokes and force-balance equations.

At the lower part of the piston, the displacer cylinder contains a slide bearing (subscript 'b'), with working fluid as a lubricant, to fix the radial position of the displacer piston and guide this as it moves vertically inside the cylinder. The leakage flow U_{l} is diverted into two narrow channels (not an annulus) and behaves like liquid columns (subscript 'b,l') as modelled elsewhere in the engine. However, there is no oscillating hydrostatic pressure difference across this component and, hence, no corresponding capacitance. The piston in the slide bearing (subscript 'b,p') consists of an inductance and resistance (derived from a force balance) which describe the drag that results from the movement of the piston and the linear velocity profile of the lubricating film. Eventually, one arrives at the components from Fig. 9 and defined in Eq. 6.

$$
\begin{aligned}
R_{\mathrm{l},1} &= \frac{128c_2h_{\mathrm{p}}\mu}{\pi c_1 c_3}\,, \quad R_{\mathrm{l},2} = \frac{128c_2h_{\mathrm{p}}\mu}{\pi c_1(c_1 - 2c_2{d_{\mathrm{p}}}^2)}\,,\\
C_{\mathrm{l}} &= \frac{\pi^2 c_1(c_1 - c_2{d_{\mathrm{p}}}^2)}{64{c_2}^2 k_{\mathrm{ms}}}\,, \quad L_{\mathrm{l}} = \frac{64{c_2}^2 m_{\mathrm{p}}}{\pi^2 c_1(c_1 - 2c_2{d_{\mathrm{p}}}^2)}\,,\\
C_{\mathrm{p}} &= \frac{\pi^2 {d_{\mathrm{p}}}^2 c_1}{32k_{\mathrm{ms}}c_2}\,, \quad R_{\mathrm{p}} = \frac{64h_{\mathrm{p}}\mu}{\pi {d_{\mathrm{p}}}^2 c_1}\,, \quad L_{\mathrm{p}} = \frac{32c_2 m_{\mathrm{p}}}{\pi^2 {d_{\mathrm{p}}}^2 c_1}\,,\\
R_{\mathrm{b,p}} &= \frac{16l_{\mathrm{b}}\mu}{\pi^2\delta {d_{\mathrm{p}}}^3}\,, \quad L_{\mathrm{b,p}} = \frac{4\rho_{\mathrm{ss}}l_{\mathrm{b}}}{\pi {d_{\mathrm{p}}}^2}\,.
\end{aligned}
\tag{6}
$$

In Eq. 6, d_c and d_p are the average diameters of the cylinder and piston, h_p is the height of the piston, μ is the dynamic viscosity of the working fluid, m_p is the mass of the piston, k_{ms} is the constant of the mechanical spring, $c_1 = {d_c}^2 - {d_p}^2$, $c_2 = \ln(d_c/d_p)$ and $c_3 = c_2(d_c^2 + d_p^2) - c_1$ are geometric constants, l_b is the length of the slide bearing, ρ_{ss} is the density of the piston (stainless steel) and $\delta \approx 0.1$ mm is the thickness of the lubricating film in the slide bearing.

3.3. Load model

To assess the performance (e.g., efficiency and power output) of the ERPE, a load must be included in the circuit model. This can be done by introducing a linear resistance at the physical location where energy can be dissipated, which can be considered as representing useful work [19–24]. However, if one wants to use data from the BIC prototype tests as indicative values for comparison and validation of the ERPE model, the model must capture the behaviour of the actual load of the BIC experimental prototype (in fact, a check-valve arrangement) as closely as possible. Pressure measurements upstream and downstream of the adjustable load valve have been performed at the BIC. These indicate that this valve cannot be accurately represented by a simple resistance. Figure 10 depicts the ratio of the amplitudes of the measured pressures downstream and upstream of the valve $|P_{down}/P_{up}|$ in the frequency domain acquired with an FFT algorithm. A single resistance would return an approximately constant amplitude ratio for all frequencies. In Fig. 10, the region in the vicinity of the oscillation frequency observed by the prototype while the measurements were performed (0.2 Hz) is of particular interest. The spectral data is found to follow the trend:

$$\frac{P_{down}}{P_{up}} = \xi \frac{1 + s\lambda_1}{1 + s\lambda_2}\,, \tag{7}$$

which is also represented in Fig. 10. In Eq. 7, $s = i\omega$ is the Laplace variable which is in this case purely imaginary as the measurements are carried out while the engine is oscillating at marginal stability. In addition, ξ, λ_1 and λ_2 are constants that are fitted such that the relation follows the spectral distribution as closely as possible in the vicinity of the oscillation frequency.

Furthermore, pressure drop measurements across the load valve, when applying steady (non-oscillating) flows, can be used to calculate a steady-flow resistance R_{sf} value with:

$$(P_{up} - P_{down}) = R_{sf} U\,, \tag{8}$$

where R_{sf} is the experimentally measured steady-flow resistance which depends solely on the valve setting and not on the operating frequency. It is the resistance to *steady flow* due to viscous drag in the valve. Equation 8 can then be rewritten in the form:

$$(P_{up} - P_{down}) \left[\frac{1 + s\lambda_2}{\xi(1 + s\lambda_1)}\right] = U \underbrace{R_{sf} \left[\frac{1 + s\lambda_2}{\xi(1 + s\lambda_1)}\right]}_{R_0}\,. \tag{9}$$

In Eq. 9, R_0 is a yet to be determined constant with the same unit as R_{sf}. Solving Eq. 7 for P_{down} and substituting the solution into the left hand side of Eq. 9 leads to:

$$(P_{\mathrm{up}} - P_{\mathrm{down}}) \left[\frac{1 + s\lambda_2}{\xi(1 + s\lambda_1)} \right] = \frac{P_{\mathrm{up}}}{\xi} \left[\frac{1 + s\lambda_2}{1 + s\lambda_1} - \xi \right] . \tag{10}$$

The expression on the left-hand side in the square brackets in Eqs. 9 and 10 is dimensionless, therefore these equations can be written in the form $\frac{1}{Z}P = U$:

$$(P_{\mathrm{up}} - P_{\mathrm{down}}) \frac{1}{R_0} \left[\frac{1 + s\lambda_2}{\xi(1 + s\lambda_1)} \right] = (P_{\mathrm{up}} - 0) \frac{1}{\xi} \frac{1}{R_0} \left[\frac{1 + s\lambda_2}{1 + s\lambda_1} - \xi \right] = U \, , \tag{11}$$

which can be rewritten as:

$$\frac{P_{\mathrm{up}} - P_{\mathrm{down}}}{Z_{\mathrm{lo},1}} = \frac{P_{\mathrm{up}} - 0}{Z_{\mathrm{lo},1} + Z_{\mathrm{lo},2}} = U \, , \tag{12}$$

where $Z_{\mathrm{lo},1}$ is the impedance describing the load and $Z_{\mathrm{lo},2}$ is the impedance describing all the components downstream of the load:

$$Z_{\mathrm{lo},1} = \xi R_0 \frac{1 + s\lambda_1}{1 + s\lambda_2} \, , \quad Z_{\mathrm{lo},2} = \xi^2 R_0 \frac{(1 + s\lambda_1)^2}{(1 + s\lambda_2 - \xi(1 + s\lambda_1))(1 + s\lambda_2)} \, . \tag{13}$$

Finally, R_0 is evaluated from Eq. 9 for $s \to 0$. Thus:

$$R_0 = \frac{R_{\mathrm{sf}}}{\xi} \, . \tag{14}$$

In the above relationships, the load impedance $Z_{\mathrm{lo},1}$ equals the steady-flow resistance R_{sf} if there is no oscillation ($s = 0$). Note that $P_{\mathrm{up}} - 0$ is the pressure drop across the load valve *and* the whole working cylinder including the gas spring. Therefore, the sum $Z_{\mathrm{lo},1} + Z_{\mathrm{lo},2}$ accounts for the components (resistors, inductors and capacitors) of everything downstream (to the left) of the upstream pressure sensor in Fig. 8 (mainly the working cylinder). The implementation of the load model of Eq. 12 in the electrical circuit is done by placing the two impedances in series, as is highlighted in Fig. 7(b).

3.4. Liquid column below piston

The section at the bottom of the displacer cylinder is modelled by defining a control volume of fixed size moving vertically with the solid piston. This defines a control volume that contains a time-varying mass that consists of the fluid (always in the liquid phase) under the solid piston, while accounting for the different average speeds of the flow and piston. The force balance for this section takes the form:

$$\begin{aligned} m_{\mathrm{d,b}} a_{\mathrm{d,b}} = & P_{\mathrm{d,b}} A_{\mathrm{d,b}} - S_{\mathrm{d,b}} \mu \left. \frac{\mathrm{d}u}{\mathrm{d}r} \right|_{\mathrm{r=r_c}} - \\ & - m_{\mathrm{d,b}} g + (u_{\mathrm{rel,in}} - u_{\mathrm{rel,out}}) \frac{\mathrm{d}m_{\mathrm{dl,b}}}{\mathrm{d}t} \, , \end{aligned} \tag{15}$$

where the subscript 'd,b' denotes values for the liquid column in the displacer cylinder below the piston. So, e.g., $m_{\mathrm{d,b}}$ is the (variable) mass of the liquid column in the control volume, $a_{\mathrm{dl,b}}$ is its acceleration, $A_{\mathrm{d,b}}$ is the cross-section area, $S_{\mathrm{d,b}}$ is the lateral area equal to the surface area of the cylinder, $\mathrm{d}u/\mathrm{d}r|_{\mathrm{r=r_c}}$ is the velocity gradient at the cylinder wall ($r = r_{\mathrm{c}}$) and u_{rel} is the velocity of incoming/outgoing flow (averaged across the cross-section area) relative to the velocity of the liquid column. The final term of the force balance accounts for the momentum of the mass being introduced into or out of the control volume. The relative velocities are given by $u_{\mathrm{rel,in}} = u - u_{\mathrm{p}}$ and $u_{\mathrm{rel,out}} = u_{\mathrm{l}} - u_{\mathrm{p}}$ where u is the velocity of the liquid flowing into the control volume which also equals the velocity of the liquid-vapour interface at the top of the displacer cylinder. The velocity of the solid piston is u_{p} and u_{l} is the area-averaged velocity of the working fluid. Since the boundary of the variable mass control volume is moving with the piston, the velocity of the liquid column also equals u_{p}. Flow losses at sudden contractions and expansions are neglected as the flow is considered to be quasi-steady, viscous laminar and fully developed flow (low Reynolds and Womersley numbers). Linearizing the equation, writing in terms of an equilibrium length $l_{\mathrm{d,b}}$, rearranging and taking the Laplace transform results in a relationship of the pressure drop to the flow-rate U:

$$\begin{aligned} P_{\mathrm{d,b}} = & \left(\frac{128\mu l_{\mathrm{d,b}}}{\pi d_{\mathrm{d,b}}^4} + \frac{\rho_{\mathrm{wf}} g}{s} \frac{1}{A_{\mathrm{p}}} \frac{Z_{\mathrm{pl}}}{Z_{\mathrm{p}}} + \right. \\ & \left. + s\rho_{\mathrm{wf}} l_{\mathrm{d,b}} \left(\frac{1}{A_{\mathrm{p}}} \frac{Z_{\mathrm{pl}}}{Z_{\mathrm{p}}} + \frac{1}{A_{\mathrm{l}}} \frac{Z_{\mathrm{pl}}}{Z_{\mathrm{l}}} - \frac{1}{A_{\mathrm{d,b}}} \right) \right) U \,. \end{aligned} \tag{16}$$

3.5. Liquid column above piston

Similarly to the treatment of the section below the solid piston, the liquid column above it is modelled by defining a control volume with a time-varying mass. However, in this case, the top and bottom boundaries of the liquid column are both moving independently of each other. The upper boundary is located at the liquid-vapour interface moving with velocity u and the lower boundary is located at the top of the piston moving with velocity u_{p}. The force balance on this region is written in a similar manner to that for the liquid column below the piston (in the previous section):

$$m_{\mathrm{d,a}} a_{\mathrm{d,a}} = P_{\mathrm{d,a}} A_{\mathrm{d,a}} - S_{\mathrm{d,a}} \mu \left. \frac{\mathrm{d}u}{\mathrm{d}r} \right|_{\mathrm{r=r_c}} - m_{\mathrm{d,a}} g + (u_{\mathrm{rel,in}}) \frac{\mathrm{d}m_{\mathrm{d,a}}}{\mathrm{d}t} \,. \tag{17}$$

The subscript 'd,a' denotes here values relating to the liquid column in the displacer cylinder above the piston, and u_{rel} is the velocity of the incoming flow relative to the velocity of the column u. Applying the same steps as in the last section leads to the expression:

$$\begin{aligned} P_{\mathrm{d,a}} = & \left(\frac{128\mu l_{\mathrm{d,a}}}{\pi d_{\mathrm{d,a}}^4} + \frac{\rho_{\mathrm{wf}} g}{s} \left(\frac{1}{A_{\mathrm{d,a}}} - \frac{1}{A_{\mathrm{p}}} \frac{Z_{\mathrm{pl}}}{Z_{\mathrm{p}}} \right) + \right. \\ & \left. + s\rho_{\mathrm{wf}} l_{\mathrm{d,a}} \left(\frac{2}{A_{\mathrm{d,a}}} - \frac{1}{A_{\mathrm{p}}} \frac{Z_{\mathrm{pl}}}{Z_{\mathrm{p}}} - \frac{1}{A_{\mathrm{l}}} \frac{Z_{\mathrm{p}}}{Z_{\mathrm{l}}} \right) \right) U \,. \end{aligned} \tag{18}$$

Equations 16 and 18 obtained for the liquid column above and below the solid piston are added together to get the total pressure drop across the entire liquid column in the displacer cylinder (excluding the piston) which can be written in terms of a set of RLC parameters as:

$$R_{\mathrm{d}} = \frac{128\mu}{\pi}\left(\frac{l_{\mathrm{d,a}}}{d_{\mathrm{d,a}}^4} + \frac{l_{\mathrm{d,b}}}{d_{\mathrm{d,b}}^4}\right), \qquad C_{\mathrm{d}} = \frac{A_{\mathrm{d,a}}}{\rho_{\mathrm{wf}} g}, \tag{19}$$

$$\begin{aligned} L_{\mathrm{d}} =& \rho_{\mathrm{wf}}\left(l_{\mathrm{d,a}}\left(\frac{2}{A_{\mathrm{d,a}}} - \frac{1}{A_{\mathrm{p}}}\frac{Z_{\mathrm{pl}}}{Z_{\mathrm{p}}} - \frac{1}{A_{\mathrm{l}}}\frac{Z_{\mathrm{p}}}{Z_{\mathrm{l}}}\right) + \right. \\ & \left. + l_{\mathrm{d,b}}\left(\frac{1}{A_{\mathrm{p}}}\frac{Z_{\mathrm{pl}}}{Z_{\mathrm{p}}} + \frac{1}{A_{\mathrm{l}}}\frac{Z_{\mathrm{pl}}}{Z_{\mathrm{l}}} - \frac{1}{A_{\mathrm{d,b}}}\right)\right). \end{aligned} \tag{20}$$

3.6. Solution

Two different heat exchanger descriptions are investigated which either account for: (1) a linear temperature profile (LTP) along the height of the heat exchanger wall; or, (2) the dynamic behaviour of the heat exchangers (DHX). In the former model, the heat exchanger walls are thermally static and have temporally constant spatial temperature profiles. In the latter, the heat exchangers can interact thermally with the working fluid and an external heat source and sink, and they have a finite capacity for periodically storing and releasing heat. The electrical circuits for each case are shown in Fig. 7, and the parameter definitions and the nominal values of each electrical model parameter (for the engine with and without a load) can be found in Table 1. Details on these models and their solution methods can be found in Refs. [21, 22].

As in Refs. [19–23], Kirchhoff's laws are applied to determine a forward path transfer function $G(s)$ relating the heat exchanger temperature represented by the pressure P_{th} (input) to the hydrostatic pressure in the displacer cylinder P_{d} (output). To close and solve the system, a feedback relation is required, namely $P_{\mathrm{th}} = k_i P_{\mathrm{d}}$. For the LTP model, the feedback gain is $k_i = k_{\mathrm{LTP}} = (\mathrm{d}T_{\mathrm{hx}}/\mathrm{d}y)\rho_{\mathrm{wf}} g(\mathrm{d}T/\mathrm{d}P)_{\mathrm{sat}}$ and for the DHX model the gain is $k_i = k_{\mathrm{DHX}}/s = (\mathrm{d}\dot{Q}_{\mathrm{hx}}/\mathrm{d}y)/g\rho_{\mathrm{v}}\Delta s_{\mathrm{fg}} T_0 C_{\mathrm{hx}} s$ [21, 22]. The gain k is proportional to the constant temperature gradient $\mathrm{d}T_{\mathrm{hx}}/\mathrm{d}y$ imposed on the heat exchanger walls in the LTP model, while in the DHX model the gain is proportional to the constant heat-input rate gradient $\mathrm{d}\dot{Q}_{\mathrm{hx}}/\mathrm{d}y$. A sustained oscillation of the engine can be observed at marginal stability of the closed-loop transfer function $C(s) = G(s)/(1-k_i G(s))$. Marginal stability occurs when one conjugate complex pole pair of the closed-loop transfer function $C(s)$ lies on the imaginary axis and all other conjugate pairs have negative real parts [19–23]. In the present work, a mathematical solver using an iterative method is used to calculate the feedback gain necessary for marginal stability. The frequency of the marginal poles is the oscillation frequency of the engine. The values of the temperature gradient $\mathrm{d}T_{\mathrm{hx}}/\mathrm{d}y$ and the heat input rate gradient $\mathrm{d}\dot{Q}_{\mathrm{hx}}/\mathrm{d}y$ are estimated from the gains, the working fluid properties listed in Table 2 and R_{th} and C_{hx} from Table 1.

It should be noted that the ERPE model (and device) lacks an external input to the engine. Instead, the input to the engine (defined here as the heat-source/sink temperature) arises and is set by an internal feedback coupling (connection) to the engine's output (defined as the oscillation of the liquid in the displacer cylinder); specifically, the heat-source temperature experienced by the working fluid as it changes phase is

set by the vertical position of the liquid level (liquid-vapour interface) in the displacer cylinder. Owing to this internal feedback connection and lack of an external input, the linear ERPE model can only result in sinusoidal oscillations of all thermodynamic properties (P, V, T) over the cycle and also of the volumetric flow-rates throughout the engine. Oscillations which contain more than one frequency component can only be attained by non-linearities within the device itself [23].

Finally, the exergy efficiency can be calculated with the following formula [19–23]:

$$\eta_{\mathrm{ex}} = \frac{\overline{P_{\mathrm{lo},1}(t)U(t)}}{\overline{T_{\mathrm{hx}}(t)\dot{S}_{\mathrm{hx}}(t)}} = \frac{\overline{P_{\mathrm{lo},1}(t)U(t)}}{\overline{P_{\mathrm{th}}(t)U_{\mathrm{th}}(t)}} = \left|\frac{P_{\mathrm{lo},1}}{P_{\mathrm{th}}}\right|^2 \frac{\mathrm{Re}(1/Z_{\mathrm{lo},1})}{\mathrm{Re}(1/Z_{\mathrm{tot}})}\,. \tag{21}$$

Table 2: Working fluid properties; saturated water at a mean pressure of 18.1 bar.

ρ_{wf}	Working fluid density	9.95×10^2 kg/m^3
ρ_{v}	Vapour density	9.13 kg/m^3
μ	Dynamic viscosity, water	7.19×10^{-4} kg/s·m
γ_{v}	Ratio of specific heats, vapour	1.46
Δs_{fg}	Entropy of vaporization	3.97×10^3 J/K·kg
$\left(\frac{\mathrm{d}T}{\mathrm{d}P}\right)_{\mathrm{sat}}$	Change in saturation temperature with pressure in two-phase region	$2.69{\times}10^{-5}$ K/Pa

4. Results and Discussion

As a first step, results from the ERPE circuit model presented in the previous sections are compared qualitatively to available experimental data from the similar, but not identical, BIC two-phase TFO for the purpose of validation (that, like the ERPE features a vertically reciprocating solid piston). The BIC prototype differs from the ERPE in that: (1) it possesses a valve in the displacer cylinder which opens depending on the piston position; (2) it can only produce work during one half-cycle owing to the load arrangement employed in the tests; and, (3) the piston does not necessarily always remain fully immersed underneath the water level inside the displacer cylinder. These factors cannot be added to our present ERPE circuit model because they are inherently and strongly nonlinear, and thus cannot be modelled linearly with acceptable accuracy. Both engines are nonetheless similar enough in all other aspects so that our calculations should lie in the same order of magnitude and reveal the same underlying trends observed in the measurements.

4.1. Comparison of model and experiments

The BIC prototype was tested under eight different operating conditions—three without and five with a load—which are summarized in Table 3. No temperature or heat transfer measurements were carried out along the walls of the heat exchangers. Therefore, no precise experimental values exist of the temperature gradient $\mathrm{d}T_{\mathrm{hx}}/\mathrm{d}y$ (required by the LTP model) or the heat-input rate gradient $\mathrm{d}\dot{Q}_{\mathrm{hx}}/\mathrm{dy}$ (required by the DHX model) applied onto the inner heat exchanger walls. Nevertheless, we are able to approximate their values based on the measured flow-rates of air and fuel and the measured temperatures at the outer wall of the heat exchangers. It is known that 465 W of thermal energy is transferred to the outer walls of the

hot heat exchanger in the three load-free cases, while 270 W is transferred to the heat exchanger in the remaining five cases with a load. The wall temperature measured at the top of the hot heat exchanger is approximately 600 °C and approximately 20 to 40 °C at the bottom of the cold heat exchanger. A linear profile is an acceptable first approximation across a portion of the heat exchanger height centred around the equilibrium position; in our case, it is assumed to be between 30 and 150 mm (instead of the 230 mm of the entire heat exchanger height). The lower height of 30 mm was chosen because the average amplitude of the oscillation height in several BIC prototype tests was around 30 mm. The results in the gradient values are listed in Table 3.

Table 3: Left: operating conditions, experimentally measured frequency and empirically approximated gradients of BIC prototype. Right: calculated frequencies and temperature/heat-input rate gradients of the LTP and DHX model.

BIC prototype operating conditions		BIC prototype measurements			LTP model			DHX model		
	Mean pressure [bar]	f [Hz]	$\mathrm{d}T_{\mathrm{hx}}/\mathrm{d}y$ [K/cm]	$\mathrm{d}\dot{Q}_{\mathrm{hx}}/\mathrm{d}y$ [W/cm]	f [Hz]	$\mathrm{d}T_{\mathrm{hx}}/\mathrm{d}y$ [K/cm]	η_{ex} [%]	f [Hz]	$\mathrm{d}\dot{Q}_{\mathrm{hx}}/\mathrm{d}y$ [W/cm]	η_{ex} [%]
no load	3.6	0.6	≈40-200	≈60-300	6.5	192	-	1.1	190	-
	5.5	0.4			7.3	198	-	1.3	206	-
	8.2	0.6			8.5	199	-	1.6	289	-
load	9.4	0.02	≈40-200	≈35-180	1.7	122	1.5	2.0	167	0.3
	11.8	0.16			2.3	115	3.3	2.5	123	1.1
	15.8	0.24			2.5	75	7.0	2.7	139	1.6
	18.1	0.29			2.7	168	2.4	2.9	147	2.0
	22	0.2			2.2	153	1.5	2.5	160	0.01

Modelling predictions of the frequency f, temperature gradient $\mathrm{d}T_{\mathrm{hx}}/\mathrm{d}y$ for the LTP model, heat input rate gradient $\mathrm{d}\dot{Q}_{\mathrm{hx}}/\mathrm{d}y$ for the DHX model, and exergy efficiency η_{ex} are also listed in Table 3. Beginning with the load-free case, it can be seen that the DHX model predicts frequencies which are two or three times higher than the direct experimental observations on the BIC prototype. Given the first-order approximate nature with which the ERPE has been modelled and the differences between the ERPE model and actual BIC arrangement on which the experiments were performed, this discrepancy is considered reasonable. The LTP model overestimates the frequency to a greater extent. Both models reasonably predict the temperature gradient or heat input rate gradient in the measurement range from Table 3. Thus, the DHX model is considered here a more accurate representation of the physical device in the load-free case compared to the LTP model, indicating that the heat exchanger walls are thermally dynamic.

In the remaining five cases in Table 3, a load is present at different pressures, and in these cases the DHX and LTP models predict similar operational oscillation frequencies which are too high, especially at low pressures. It is possible that, despite the present effort, the introduction of the non-linear valve load arrangement in the prototype is not properly captured in the present model. Both models, however, do capture the trend of the operation frequency increasing with the mean pressure before decreasing again at

the highest pressure of 22 bar. Furthermore, as with the load-free cases, the temperature and heat input rate gradients are within the measured ranges for both models. On the other hand, the models differ significantly in their estimations of the exergetic efficiency, with the DHX predicting lower values. The LTP predicts efficiencies between 1.5% and 7% while the DHX efficiencies are between 0.01% and 2%. Nonetheless, both models predict low efficiencies at the lowest and highest pressures (9.4 and 22 bar), while the higher efficiencies are attained at intermediate pressures (15.8 bar). It must be noted, however, that we do not have measurements which can provide experimental efficiency values for comparison. In conclusion, the DHX model is considered in this work a reasonable first description of what would be expected from a heat exchanger arrangement in a possible physical representation of an ERPE device.

4.2. Parametric study

In this section, the influence of the various electrical ERPE model parameters (RLC) on the: (a) operational/oscillation frequency f, (b) exergy efficiency η_{ex} (with a load), (c) heat-input rate gradient $\mathrm{d}\dot{Q}_{\mathrm{hx}}/\mathrm{d}y$, and (d) product of exergy efficiency and frequency $\eta_{\mathrm{ex}} \times f$ (with a load) are examined for two engine configurations: (a) a load-free configuration at a time-averaged mean pressure of 3.6 bar that matches the lowest no-load pressure case in Table 3, and (b) an engine configuration featuring a load with an 18.1 bar mean pressure that matches the highest (DHX) efficiency load case in Table 3. The product of exergy efficiency and frequency $\eta_{\mathrm{ex}} \times f$ is proportional to the hydraulic power output per unit heat input, and therefore high values for this product are favourable. Similarly, low heat-input rates/temperature gradients are also favourable because they are measures of the thermal input/temperature difference required to sustain the operation of the device. Each RLC parameter considered here is directly linked to the geometric, thermodynamic/thermophysical or transport properties of the ERPE that result from solid materials and/or fluid substance selection decisions and the operational characteristics of the device, as defined in Table 1.

The results of this parametric exercise can be found in Figs. 1 and 2, where only influential parameters are shown and parameters with negligible influence have been omitted. In these figures, the RLC parameters are given in normalized form (e.g., R^*_{th}) meaning that the varied parameters (e.g., R_{th}) are divided by their respective nominal values (e.g., $R_{\mathrm{th,nom}}$). The nominal values are based on pre-defined geometric, thermodynamic/thermophysical and transport properties taken from the BIC prototype (see Table 1) in order to give the model a physically realisable starting point for this exercise. The considered variation range for each parameter is between 10^{-3} and 10^{3} times the nominal starting value.

Beginning with the operational frequency of a load-free ERPE shown in Fig. 1(a), the three most influential parameters are the capacitance of the argon gas spring in the working cylinder C_{g}, the capacitance of the vapour-phase gas spring at the top of the displacer cylinder C_{v} and the inductance of the liquid in the connection tube L_{c} (see Fig. 8). All other parameters, including C_{d}, C_{hx} and R_{th} that are also shown in Fig. 1(a), have very little influence on the frequency of the ERPE.

The inductance L_{c} has the largest magnitude of all the inductances in the model while the two gas-spring capacitances C_{v} and C_{g} have the smallest magnitudes of all the capacitances. Dominant capacitances have

small values because the corresponding impedance is given by $Z = 1/sC$. Therefore, changes to these three parameters appear to have the greatest influence on the frequency of the ERPE as a whole. To maximize the frequency, the two gas-spring capacitances must be reduced as much as possible. Reducing the capacitances of the gas springs is analogous to decreasing the time-mean dead volumes in these parts of the device. The dependency on L_c also suggests the implementation of a reduced connection-tube inductance. Table 1 suggests measures that can be taken in the desired direction; to reduce this inductance, the cross-sectional area of the connection tube must be increased and/or the length of the tube must be shortened.

Figure 1(b) shows the heat input rate gradient $\mathrm{d}\dot{Q}_\mathrm{hx}/\mathrm{d}y$ as a function of: the hydrostatic capacitance in the displacer cylinder C_d, the working cylinder gas-spring C_g, the heat exchanger capacitance C_hx, the vapour gas-spring capacitance C_v, the connection-tube inductance L_c and the thermal resistance R_th. With the exception of C_d and L_c, reducing all of these parameters below the nominal design values defined by the BIC prototype by approximately one order of magnitude (but not much further), leads to an advantageous reduction in the necessary heat-input requirement. The thermal-domain parameters, heat-exchanger capacitance C_hx and thermal resistance R_th, attain a minimum heat-input at slightly lower values. The thermal resistance R_th is inversely proportional to the heat-transfer area and the heat transfer coefficient of phase change, so increasing these (e.g., through the addition of fins, etc. [30]) reduces the thermal resistance. Also, the heat-exchanger capacitance C_hx depends proportionally on the heat capacity c_hx of the heat exchanger material and the mass m_hx of the portion of the heat exchangers which interacts thermally with the working fluid. To reduce these, a heat exchanger material can be used which has a lower specific heat capacity.

The two most dominant parameters are the hydrostatic capacitance in the displacer cylinder C_d with which the necessary heat input $\mathrm{d}\dot{Q}_\mathrm{hx}/\mathrm{d}y$ increases linearly (in this log-log plot), and the inductance of the liquid in the connection tube L_c which allows low heat inputs when increased by at least a factor of $\sim$100 from its nominal value. According to Eq. 3, these effects can be achieved in practice by a decrease in the cross-sectional area of the displacer cylinder, and therefore a decrease in the quantity of working fluid per unit height of the heat exchanger (requiring less thermal energy for evaporation per unit height), which decreases the corresponding hydrostatic capacitance (C_d). The only significant inductance L_c can be increased, for example, by lengthening the connection tube or using a smaller tube diameter.

Figure 1(b) also shows sharp inflection points or discontinuities in the trends of C_g, C_v and L_c. As explained in Section 3.6, the closed-loop transfer function has seven poles: one real and three complex conjugate pairs. For marginal stability, one of these pairs is purely imaginary while the others have negative real parts. At the discontinuities, the dominant pair of poles switches to a different pair which leads to a sudden change in the oscillating frequency and gain, and hence the heat transfer rate gradient. Discontinuities have also been observed in previous linearized modelling studies of the NIFTE [22, 23].

A similar parametric study is carried out for an ERPE engine but now with a load and a mean pressure of 18.1 bar. The influence of various parameters on the performance indicators (frequency f, exergy efficiency η_ex, heat-input rate gradient $\mathrm{d}\dot{Q}_\mathrm{hx}/\mathrm{d}y$ and the product $\eta_\mathrm{ex} \times f$) is examined. Of the 19 variable parameters

for the load case (see Fig. 7(b)), only five influence the performance indicators significantly, namely the thermal resistance R_{th}, the heat exchanger capacitance C_{hx}, vapour compressibility in the displacer cylinder C_{v}, the hydrostatic capacitance in the displacer cylinder C_{d} and the inductance of the connection tube L_{c}. All other parameters affect the performance indicators only marginally, even if they are varied by several orders of magnitude. Figure 2 summarizes the relevant results from this parametric study.

Similarly to the load-free case, the two heat exchanger parameters R_{th} and C_{hx} influence the frequency in a similar manner, as shown in Fig. 2(a). When reduced below their nominal values, these two parameters lead to a monotonic increase in the frequency within the entire investigated parameter ranges. Furthermore, as with the load-free case, a low vapour-spring capacitance C_{v} results in a significantly higher frequency, as does a low connection-tube inductance L_{c} although to a smaller extent.

The exergetic efficiency in Fig. 2(b) is mainly influenced by the vapour-spring capacitance C_{v} and, to a lesser extent, the connection-tube inductance L_{c}. Reducing the capacitance C_{v} leads to a substantial increase in the efficiency, which is shown to reach theoretical values up to 90%, while increasing L_{c} to approximately 100 times its nominal value increases the efficiency from 2% to 20%. The remaining three parameters discussed here only alter the efficiency by a few percentage points. Although the ERPE has low efficiencies at the nominal values derived from the BIC prototype, Fig. 2(b) shows that it is possible with relatively simple measures to substantially increase the efficiency (this can also be said of the frequency). Increasing the pressure or reducing the volume of the vapour region in combination with increasing the length of the connection tube and reducing its diameter would increase the efficiency. In Fig. 2(b), the ERPE demonstrates a potential of exhibiting high exergetic efficiencies, and it is not expectd to be advsersely affected by the same degree of parasitic condensation that has been observed in the NIFTE [21]. The remaining of the five aforementioned parameters, C_{d}, C_{hx} and R_{th}, have little to no effect on the exergy efficiency.

Figure 2(c) shows the behaviour of the necessary heat input rate gradient $\mathrm{d}\dot{Q}_{\mathrm{hx}}/\mathrm{d}y$. The thermal resistance R_{th}, the heat exchanger capacitance C_{hx} and the vapour compressibility C_{v} all show a similar trend: the necessary heat input reaches a minimum for values slightly below the employed nominal values. Once again, the most influential parameter is the hydrostatic capacitance in the displacer cylinder C_{d} with which the necessary heat input $\mathrm{d}\dot{Q}_{\mathrm{hx}}/\mathrm{d}y$ increases as a power law (approximately linearly in the log-log plot) for the entire range of investigated values around the nominal BIC design. Furthermore, $\mathrm{d}\dot{Q}_{\mathrm{hx}}/\mathrm{d}y$ decreases to a minimum at an L_{c} value of around 100 times its nominal value.

The final plot in Figure 2(d) shows the behaviour of the hydraulic power output per unit heat input. Changing the inductance L_{c} has a comparatively small effect on the normalized power output while changes in C_{d} have almost no effect. The normalized power output is maximized for values of the thermal resistance R_{th} a little below the nominal value ($0.25 \times R_{\mathrm{th,nom}}$) and decreases for values lower and higher than that. The normalized power output also increases monotonically with the capacitance C_{hx} before levelling off around the nominal value. The most dominant parameter is the gas spring capacitance C_{v} with which the power output decreases sharply. This parameter should therefore be kept as small as possible.

4.3. Thermodynamic cycle diagrams

Figures 3 shows pressure–volume ($P_{\mathrm{lo},1}$–$V_{\mathrm{lo},1}$) diagrams at (across) the load, which relate to the useful power delivered to the load; and Fig. 4 shows temperature-entropy (T–S) diagrams at the heat exchangers of the engine, which relate to the exergy input to the device and to the working fluid, and help explain the trends of the exergy efficiency and normalized power output in Fig. 2(b) and (d). The areas enclosed by the P–V diagrams (Fig. 3) represent the net work output in one oscillation/cycle that can be multiplied with the frequency to obtain the hydraulic power. The T–S diagrams (Fig. 4) show the temperatures of the solid heat exchanger surfaces that the fluid contacts T_{hx} and of the working fluid T_{v} contained within the displacer cylinder that takes part in the thermal interaction with the heat exchangers. The areas enclosed by T_{hx} (solid or dash-dotted lines) correspond to the exergy input to the engine, and the areas enclosed by T_{v} (dashed or dotted lines) are the net exergy gained by the working fluid. Hence, the difference between the two areas is equivalent to the exergy destruction due to heat transfer to/from the working fluid during one oscillation. For all cases, the exergy input rate to the engine was kept constant and the time-averaged pressure was 18.1 bar. The five parameters from Fig. 2 are perturbed to $1/5$ and 5 times their respective nominal values, however, only those parameters which display significant variation in their respective diagrams are shown.

The P–V diagrams are in accordance with the power output trends from Fig. 2(d). Just like the power output per unit heat input, the work output per cycle increases with increasing C_{hx} and L_{c}, and with decreasing R_{th} and C_{v}. These Lissajous plots provide additional information as to what the increase in work and power output can be attributed to. An increase in area of these curves can be caused by an increase of the amplitudes of P and V, or an improvement in the phase difference between them towards an ideal of 90°. Figure 3(b), for example, shows us that when C_{v} is reduced, the area (and work output) increases due to a slight improvement of the phase difference and, more importantly, due to a significant elevation of the pressure amplitude (and not as much the displacement amplitude). For the three other parameters, both variable amplitudes (pressure and displacement) increase similarly and contribute to the overall improvement, especially for L_{c}. For this latter parameter, the area increases to a greater extent than the other parameters despite the phase difference also changing substantially (Fig. 3(c)); the phase differences are not strongly influenced by the variations to the thermal domain parameters, C_{hx} and R_{th}. For the other two parameters, the ellipse symmetry axes both steepen at lower values.

Figure 4 shows how varying C_{v} and L_{c} affects the exergy input, and thereby, the exergy efficiency. At high C_{v} values (Fig. 4(b)), the area enclosed by the Lissajous T_{hx}–S curve (which represents the external exergy input to the device) is large compared to the curve obtained with smaller values of C_{v}, primarily due to the larger amplitudes of the entropy flow-rate. On the other hand, the area enclosed by the T_{v} curve (the net exergy transferred to the working fluid) is virtually zero due to an extremely small temperature amplitude. When moving to smaller values of C_{v} (Fig. 4(a)), the phase difference between T_{v} and S increases from 16° for $5 \times C_{\mathrm{v,nom}}$ to 73° for $1/5 \times C_{\mathrm{v,nom}}$ and the amplitude of T_{v} increases as well. Simultaneously, the area enclosed by the T_{hx} curve drops considerably thanks to a sharp drop in the entropy amplitude (although the

temperature increases here also). In summary, when reducing C_{v} the two areas exhibit opposite behaviours: the T_{hx} area decreases and the T_{v} increases meaning that total exergy input to the system is smaller, while at the same the net exergy transferred to the working fluid increases. This sharp reduction in exergy destruction at the heat exchanger is the reason for the sharp increase of the exergy efficiency at lower C_{v}.

A higher L_{c} is also associated with an improvement in efficiency although the area of the T_{hx} curve enlarges. From $1/5 \times L_{\mathrm{c,nom}}$ to $5 \times L_{\mathrm{c,nom}}$, the phase difference between T_{v} and S rises from 26° to 40°, while the phase difference between T_{hx} and S decreases slightly from 90° to 85°. Additionally, the temperature and entropy amplitudes associated with the T_{v} curve increase, while for the T_{hx} curve only the entropy amplitude increases. Thus, the area enclosed by the T_{v} curve increases to a greater extent than that enclosed by the T_{hx} curve. Therefore, an improvement of the exergy efficiency is observed, however it is not as substantial as the increase made possible through variations of C_{v}, because the exergy input to sustain oscillations also increases. All other parameters show no great variations in the T–S diagrams.

In summary, an efficient and high-power engine requires: (a) a very low C_{v}, which is also the most influential parameter, (b) an R_{th} slightly below the nominal value, (c) a nominal C_{hx}, and (d) a moderately high L_{c}. Requirement (a) can be implemented with a small vapour space or a high mean pressure. This also leads to a high frequency. Furthermore, R_{th} and C_{hx} can be increased/decreased by improving/reducing the heat transfer performance or the heat transfer coefficient, whereas L_{c} is proportional to the connection tube length and inversely proportional to the tube diameter. This configuration also leads to a high frequency, however if there is a desire to increase it further, then R_{th} should be reduced instead of C_{hx} if both are at their nominal values. A decrease of C_{hx} in this case, will increase frequency but also reduce power. To keep the necessary heat input low, L_{c} should be moderately high, C_{d} should be as small as possible (small cross-section area) and all other parameters minimize the heat input slightly below their nominal values.

5. Conclusions

A first-order linearized, spatially lumped dynamic model of a class of unsteady heat-engine referred to as the 'Evaporative Reciprocating-Piston Engine' (ERPE) has been developed as an electronic circuit representation. This model applies electrical analogies founded on thermoacoustic and thermofluidic principles where combinations of resistances, inductances and capacitances can represent the operation of different physical components of an engine. The circuit was defined to potentially exhibit higher efficiencies than other two-phase thermofluidic oscillators, while it can also be used to guide the early-stage design of complex unsteady thermodynamic systems. The electronic circuit was converted into a physical representation of a concept engine which consists of two vertical cylinders, displacer and working cylinder, and a free solid piston within the former. A pair of hot and cold heat exchangers along the walls of the displacer cylinder periodically adds and extracts heat from the working fluid in this part of the engine. During the heat addition phase, working fluid evaporates, thereby increasing the pressure in the vapour space. This leads to the positive displacement of the liquid column as well as the displacer piston. As the vapour liquid interface moves down

to the cold heat exchanger, it begins condensing which reverses the aforementioned process. The working cylinder contains a liquid column and a gas spring. The inertia of the liquid columns in both cylinders, the compressibility of the gas and vapour springs as well as the hydrostatic pressure differences between both cylinders help sustain pressure and flow-rate oscillations of the working fluid which can be harvested to produce hydraulic work in a load.

An existing experimental prototype shows similarities in aspects to the physical representation of the ERPE, therefore geometric and thermodynamic parameters of the prototype are applied to it. Measurements of the frequency, temperature gradients and heat input rate gradient in the prototype are used as indicative values for the calculations of the model. The developed model contains two sub-models of the heat transfer process. One allows for a dynamic heat exchange (DHX) process to take place at the heat exchangers which accounts for the capacity of the heat exchanger walls to store and release heat. The other sub-model assumes a linear temperature profile (LTP) along the height of the heat exchanger walls. The models in all cases overestimate the frequency, but the DHX model predicts realistic frequencies in the load-free case. The temperature and heat input gradients predictions, on the other hand, are all within acceptable ranges.

Parametric studies have shown that for the load-free case, the argon gas spring compressibility C_g, vapour gas spring compressibility C_v and connection tube inductance L_c—if kept at a minimum—have the highest effect on increasing the frequency. Additionally, to minimize the heat input rate gradient, the thermal resistance R_th, heat exchanger capacitance C_hx, displacer cylinder hydrostatic capacitance C_d and vapour gas spring compressibility C_v should be low, while the connection tube inductance L_c should be high.

In an engine equipped with a load, only five parameters prove to affect the frequency, exergy efficiency, heat-input rate gradient or power output significantly: the thermal resistance R_th, the heat exchanger capacitance C_hx, the vapour compressibility C_v, the connection tube inductance L_c and the hydrostatic capacitance C_d of the displacer cylinder. The most influential parameter is C_v. To increase the power output, exergy efficiency and frequency, the vapour compressibility C_v must be as low as possible while the connection tube inductance L_c should be kept moderately high. This can be achieved by decreasing the time-averaged vapour space, increasing the mean pressure, reducing the diameter of the connection tube or increasing its length. Additionally, keeping the thermal resistance R_th and heat exchanger capacitance C_hx at intermediate (nominal) levels will further increase power output and efficiency. The resistance is inversely proportional to the heat transfer coefficient and heat transfer area, while the capacitance is proportional to the heat capacity of the walls and their mass. Finally, to keep the necessary heat input low, the parameters are optimal around their nominal values except for L_c, which should be moderately high (as before for the efficiency), and the hydrostatic capacitance in the displacer cylinder C_d, which should be as small as possible by decreasing the cross-section area of the cylinder.

The deterioration in efficiency and power output per unit heat input depending on C_v and L_c can be ascribed to an increase in required exergy input to the engine which does not translate into an increase in work output. The exergy destruction mainly occurs at the transfer of heat to the working fluid, often due to

an unfavourable phase difference. The insight from these results offers important suggestions and guidance for improving performance and for system optimization.

Acknowledgement

This research was performed under the UNIHEAT project. The authors wish to acknowledge the Skolkovo Foundation and BP for financial support. The authors would also like to thank Mr. Christoph Kirmse from the CEP Laboratory for his invaluable contribution and input.

Appendix A: Piston and Leakage Model

To derive first-order ordinary differential equations for the leakage flow and the piston motion, the Navier-Stokes equations for the flow and a force balance (Newton's second law) on the piston are applied. Figure 5 shows a schematic of the piston and leakage model. A force balance on the piston gives:

$$m_{\mathrm{p}}\ddot{z} = A_{\mathrm{p}}(P_2 - P_1) - m_{\mathrm{p}}g - kz - \mu\frac{\mathrm{d}u_z}{\mathrm{d}r}(r = \frac{1}{2}d_{\mathrm{p}})A_{\mathrm{shell}}\,, \tag{22}$$

where m_{p} is the mass and A_{p} the cross-section area of the piston, A_{shell} is the cylindrical surface on the vertical sides the piston in contact with the liquid, and z is the vertical displacement of the piston.

Since only the oscillating (fluctuating) component of the motion is considered, $z' = z - \overline{z}$, $m_{\mathrm{p}}g$ drops out of the analysis (see relevant discussion on this point in Section 3):

$$m_{\mathrm{p}}\ddot{z} = A_{\mathrm{p}}(P_2 - P_1) - kz - \mu\frac{\mathrm{d}u_z}{\mathrm{d}r}(r = \frac{1}{2}d_{\mathrm{p}})A_{\mathrm{shell}}\,, \tag{23}$$

which is an equation only for the oscillatory motion but with the primes dropped as before in Section 3.

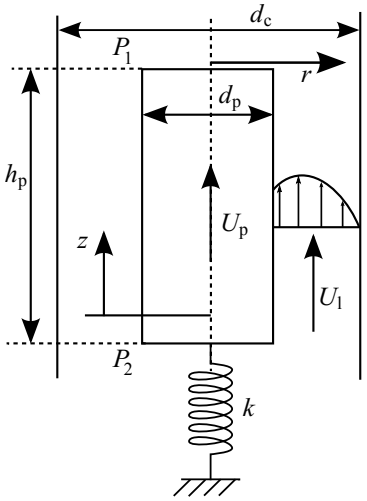

Figure 1: Schematic of piston and leakage model. The piston height is denoted by h_{p}, while d_{p} and d_{c} are the piston and cylinder diameter respectively. The pressure at the top of the piston is P_1 and P_2 at the bottom. The leakage flow is referred to as U_{l} while U_{p} is the flow-rate of the piston, and k is the spring constant.

The axial flow-component Navier-Stokes equation in cylindrical coordinates for the leakage flow is:

$$\rho\left(\frac{\partial u_z}{\partial t}+u_r\frac{\partial u_z}{\partial r}+\frac{u_\phi}{r}\frac{\partial u_z}{\partial \phi}+u_z\frac{\partial u_z}{\partial z}\right)=-\frac{\partial P}{\partial z}+\rho g+\mu\left(\frac{1}{r}\frac{\partial}{\partial r}\left(r\frac{\partial u_z}{\partial r}\right)+\frac{1}{r^2}\frac{\partial^2 u_z}{\partial \phi^2}+\frac{\partial^2 u_z}{\partial z^2}\right). \tag{24}$$

After ignoring gravity, as above, the leakage flow is assumed to be incompressible, fully developed, quasi-steady, one-dimensional and axisymmetric which simplifies the Navier-Stokes equation to:

$$\frac{1}{\mu}\frac{\partial P}{\partial z}=\frac{1}{r}\frac{\partial}{\partial r}\left(r\frac{\partial u_z}{\partial r}\right). \tag{25}$$

Solving this differential equation for the velocity $u_z = u_\mathrm{l}$ leads to:

$$u_\mathrm{l}(r)=\frac{1}{4\mu}\frac{\mathrm{d}P}{\mathrm{d}z}r^2+C_1\ln r+C_2\,. \tag{26}$$

To determine the constants C_1 and C_2, the boundary conditions at the cylinder wall $u_l(r=d_\mathrm{c}/2)=0$ and at the piston surface $u_l(r=d_\mathrm{p}/2)=4U_\mathrm{p}/\pi d_p^2$ are applied, where U_p is the volumetric flow-rate corresponding to the piston motion. After applying the boundary conditions and inserting u_l into the Navier-Stokes equation (Eq. 24), the following relation between the pressure difference across the piston and the piston flow-rate is found (after some manipulation and a Laplace transformation):

$$U_\mathrm{p}=\underbrace{\left[\frac{\pi^2 d_\mathrm{p}^2(d_\mathrm{c}^2-d_\mathrm{p}^2)s}{-32m_\mathrm{p}\ln\frac{d_\mathrm{p}}{d_\mathrm{c}}s^2+64\pi h_\mathrm{p}\mu s-32k\ln\frac{d_\mathrm{p}}{d_\mathrm{c}}}\right]}_{1/Z_\mathrm{p}}\Delta P_\mathrm{p}\,, \tag{27}$$

where s is the Laplace variable and $\Delta P_\mathrm{p}=P_2-P_1$ is the pressure drop across the piston. The fraction in front of ΔP_p can be considered the inverse of the solid piston impedance Z_p (as $\Delta P = ZU$). Finally, with partial fraction decomposition, Z_p can be rewritten as:

$$Z_\mathrm{p}=sL_\mathrm{p}+R_\mathrm{p}+\frac{1}{sC_\mathrm{p}}\,, \tag{28}$$

where L_p, R_p and C_p are described in Eq. 6. Equation 28 proves that the solid piston can be described by an inductance L_p, resistance R_p and capacitance C_p in series.

If we integrate $u_\mathrm{l}(r)$ over the annular area between the piston and cylinder, we obtain an expression for the volumetric flow-rate of the leakage flow U_l:

$$U_\mathrm{l}=\underbrace{\left[\frac{\pi\left(d_\mathrm{c}^2-d_\mathrm{p}^2\right)\left(d_\mathrm{c}^2-d_\mathrm{p}^2+\ln\frac{d_\mathrm{p}}{d_\mathrm{c}}\left(d_\mathrm{c}^2+d_\mathrm{p}^2\right)\right)}{128h_\mathrm{p}\mu\ln\frac{d_\mathrm{p}}{d_\mathrm{c}}}+\frac{s\pi^2\left(d_\mathrm{c}^2-d_\mathrm{p}^2\right)\left(d_\mathrm{c}^2-d_\mathrm{p}^2+2d_\mathrm{p}^2\ln\frac{d_\mathrm{p}}{d_\mathrm{c}}\right)}{64\ln\frac{d_\mathrm{p}}{d_\mathrm{c}}\left(m_\mathrm{p}\ln\frac{d_\mathrm{p}}{d_\mathrm{c}}s^2-2\pi h_\mathrm{p}\mu s+k\ln\frac{d_\mathrm{p}}{d_\mathrm{c}}\right)}\right]}_{1/Z_\mathrm{l}}\Delta P_\mathrm{p}\,. \tag{29}$$

Similarly to above, the inverse of the impedance of the leakage flow Z_l can be written as:

$$\frac{1}{Z_\mathrm{l}} = \frac{1}{R_{\mathrm{l},1}} + \frac{1}{sL_\mathrm{l} + R_{\mathrm{l},2} + \frac{1}{sC_\mathrm{l}}}\,, \tag{30}$$

from which it is clear that the impedance Z_l, in the electronic circuit representation, can be considered as consisting of an inductance L_l, resistance $R_{\mathrm{l},2}$, capacitance C_l in series and a resistance R_l connected in parallel to the former three as in Fig. 6. The details of the four components are given in Eq. 6. There is no physical interpretation for the division of the U_l flow into two parallel branches, or for the associated components, as there is for the rest of the engine. These interconnections and components are a result of algebraic manipulations of the coupled Navier-Stokes and force-balance equations above.

In the lower part of the piston (subscript 'b'), the leakage flow U_l is diverted into two parallel and identical channels. The fluid in these channels behaves like a liquid column and, therefore, can be modelled by using an inductance to account for the liquid's inertia $L_{\mathrm{b,l}}$ and a resistance $R_{\mathrm{b,l}}$ to represent viscous drag. These components must be placed in the U_l branch of the circuit in Fig. 6, to the right of what is shown in this figure (see Fig. 9 for the complete set of connectinos), and since there are two identical channels, there are two identical parallel such branches in the circuit. Similarly, the solid-piston movement in the slide bearing is modelled by using a resistance $R_{\mathrm{b,p}}$ in series with an inductance $L_{\mathrm{b,p}}$ to account for the friction of the piston and its inertia. These two components are placed in piston branch of the circuit U_p. Finally, one arrives at the components in Eq. 6 and the circuit representation in Fig. 9.

References

[1] C. N. Markides, The role of pumped and waste heat technologies in a high-efficiency sustainable energy future for the UK, Applied Thermal Engineering 53 (2) (2013) 197–209.

[2] C. N. Markides, Low-concentration solar-power systems based on organic Rankine cycles for distributed-scale applications: Overview and further developments, Frontiers in Energy Research 3 (2015) 47:1–16.

[3] M. Altmann, A. Brenninkmeijer, J.-C. Lanoix, D. Ellison, A. Crisan, A. Hugyecz, G. Kronedd, S. Hanninen, Decentralized energy systems, Tech. rep., European Parliament's Committee on Industry, Research and Energy (ITRE) (June 2010).
URL http://www.europarl.europa.eu/document/activities/cont/201106/20110629ATT22897/20110629ATT22897EN.pdf

[4] G. R. Simader, R. Krawinkler, G. Trnka, Micro CHP systems: State-of-the-art, Tech. rep., Austrian Energy Agency (March 2006).
URL https://ec.europa.eu/energy/intelligent/projects/sites/iee-projects/files/projects/documents/green_lodges_micro_chp_state_of_the_art.pdf

[5] A. Schuster, S. Karellas, E. Karakas, H. Spliethoff, Energetic and economic investigation of organic Rankine cycle applications, Applied Thermal Engineering 29 (8–9) (2009) 1809–1817.

[6] G. Holdmann, C.-S. Lin, J. Jensen, Test evaluation of organic Rankine cycle engines operating on recovered heat from diesel engine exhaust, Tech. rep., Alaska Energy Authority (August 2009). URL http://www.akenergyauthority.org/Content/Programs/AEEE/PDF%20files/8-27-09_AEA-RSA0925TaskOneFinalReport.pdf

[7] T. C. B. Smith, Power dense thermofluidic oscillators for high load applications, in: Proceedings of the 2nd International Energy Conversion Engineering Conference, 2004, pp. 1–15, Providence (RI), USA.

[8] C. N. Markides, A. Gupta, Experimental investigation of a thermally powered central heating circulator: Pumping characteristics, Applied Energy 110 (2013) 132–146.

[9] G. W. Swift, Thermoacoustic engines, Journal of the Acoustical Society of America 84 (4) (1988) 1145–1180.

[10] J. Wheatley, T. Hofler, G. W. Swift, A. Migliori, An intrinsically irreversible thermoacoustic heat engine, Journal of the Acoustical Society of America 74 (1) (1983) 153–170.

[11] J. Wheatley, T. Hofler, G. W. Swift, A. Migliori, Experiments with an intrinsically irreversible acoustic heat engine, Physical Review Letters 50 (7) (1983) 499–502.

[12] S. Backhaus, G. W. Swift, A thermoacoustic Stirling heat engine, Letters to Nature 399 (1999) 335–338.

[13] S. Backhaus, G. W. Swift, A thermoacoustic-Stirling heat engine: Detailed study, Journal of the Acoustical Society of America 107 (6) (2000) 3148–3166.

[14] G. W. Swift, Thermoacoustics: A Unifying Perspective for some Engines and Refrigerators, Acoustical Society of America, American Institute of Physics Press, New York, 2002.

[15] C. W. Stammers, The operation of the Fluidyne heat engine at low differential temperatures, Journal of Sound and Vibration 63 (4) (1979) 507–516.

[16] C. West, The Fluidyne heat engine, Tech. rep., United Kingdom Atomic Energy Authority (May 1971).

[17] C. D. West, R. B. Pandey, Laboratory prototype Fluidyne water pump, in: Proceedings of the 16th Intersociety Energy Conversion Engineering Conference, 1981, pp. 1916–1918, Atlanta (GA), USA.

[18] J. W. Mason, J. W. Stevens, Characterization of a solar-powered Fluidyne test bed, Sustainable Energy Technologies and Assessments 8 (2014) 1–8.

[19] C. N. Markides, T. C. B. Smith, A dynamic model for the efficiency optimization of an oscillatory low grade heat engine, Energy 36 (12) (2011) 6967–6980.

[20] R. Solanki, A. Galindo, C. N. Markides, Dynamic modelling of a two-phase thermofluidic oscillator for efficient low grade heat utilization: Effect of fluid inertia, Applied Energy 89 (1) (2012) 156–163.

[21] R. Solanki, R. Mathie, A. Galindo, C. N. Markides, Modelling of a two-phase thermofluidic oscillator for low-grade heat utilisation: Accounting for irreversible thermal losses, Applied Energy 106 (2013) 337–354.

[22] R. Solanki, A. Galindo, C. N. Markides, The role of heat exchange on the behaviour of an oscillatory two-phase low-grade heat engine, Applied Thermal Engineering 53 (2) (2013) 177–187.

[23] C. N. Markides, A. Osuolale, R. Solanki, G.-B. V. Stan, Nonlinear heat transfer processes in a two-phase thermofluidic oscillator, Applied Energy 104 (2013) 958–977.

[24] C. N. Markides, R. Solanki, A. Galindo, Working fluid selection for a two-phase thermofluidic oscillator: Effect of thermodynamic properties, Applied Energy 124 (2014) 167–185.

[25] K. Palanisamy, A. I. Taleb, C. N. Markides, Optimizing the Non-Inertive-Feedback Thermofluidic Engine for the conversion of low-grade heat to pumping work, Heat Transfer Engineering 36 (14–15) (2015) 1304–1321.

[26] P. H. Ceperley, A pistonless Stirling engine—The traveling wave heat engine, Journal of the Acoustical Society of America 66 (5) (1979) 1508–1513.

[27] T. C. B. Smith, Thermally driven oscillations in dynamic applications, Ph.D. thesis, University of Cambridge (2006).

[28] V. A. Kirillov, V. V. Kireenkov, N. A. Kuzin, A. V. Samoilov, A. B. Shigarov, Catalytic external combustion engine, Theoretical Foundations of Chemical Engineering 49 (4) (2015) 375—387.

[29] M. Glushenkov, M. Sprenkeler, A. Kronberg, V. Kirillov, Single-piston alternative to Stirling engines, Applied Energy 97 (2012) 743–748.

[30] D. Gorenflo, D. Kenning, VDI Heat Atlas: Part H2, 2nd Edition, Springer, 1993.

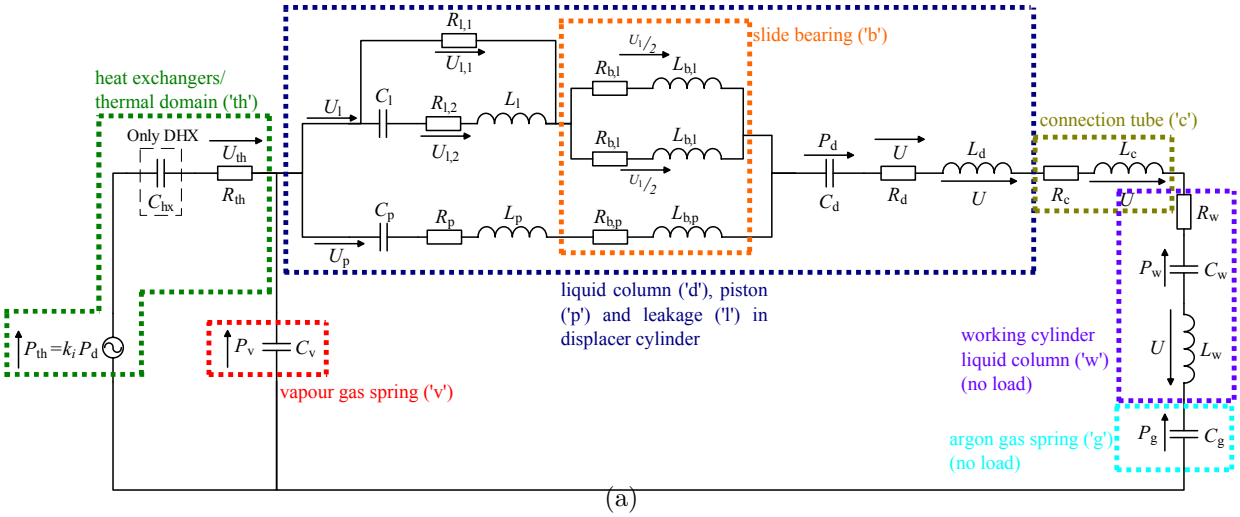

(a)

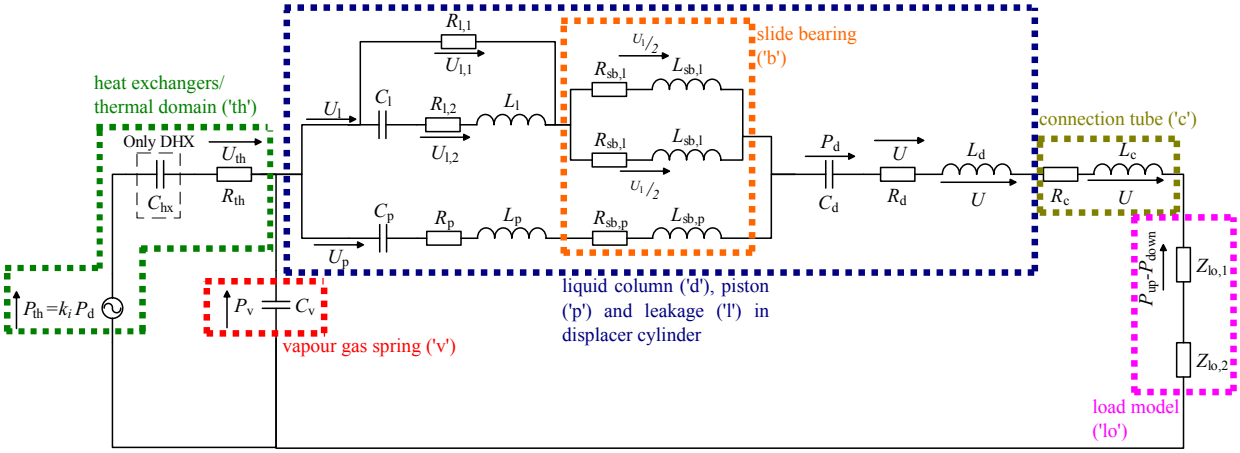

(b)

Figure 2: Electronic circuit model of the ERPE: (a) without a load; and (b) with a load. The LTP model differs from the DHX model in that it lacks the heat exchanger capacitance C_{hx}. For the LTP, the feedback gain $k_i = k_{\mathrm{LTP}}$ while for the DHX $k_i = k_{\mathrm{DHX}}/s$. The coloured, dashed borders correspond to the components highlighted in Fig. 8.

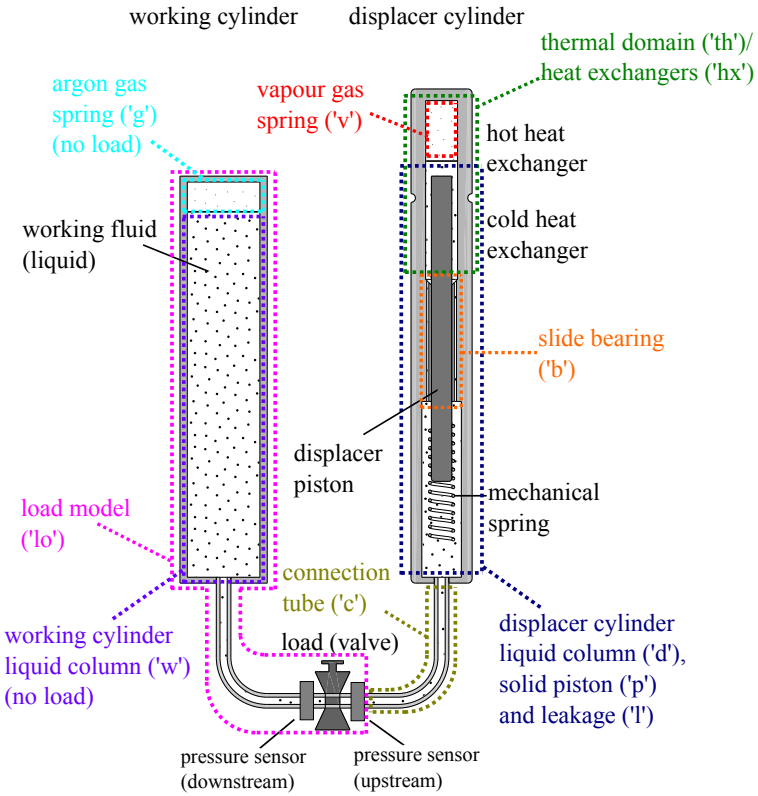

Figure 3: Schematic description of the ERPE. The dashed and coloured borders denote different components or domains of the engine; these correspond to the highlighted sections in the electronic circuits of Fig. 7.

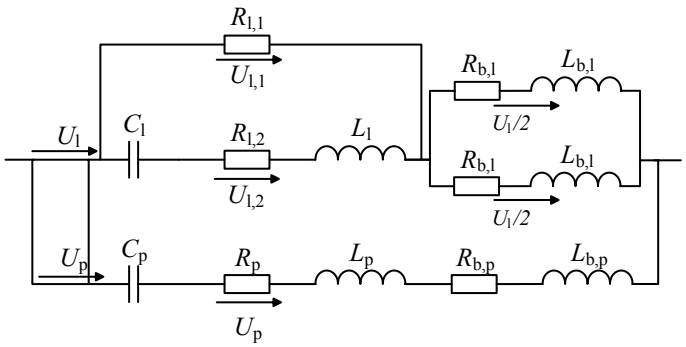

Figure 4: Electrical circuit representation of piston and leakage flow including slide bearing.

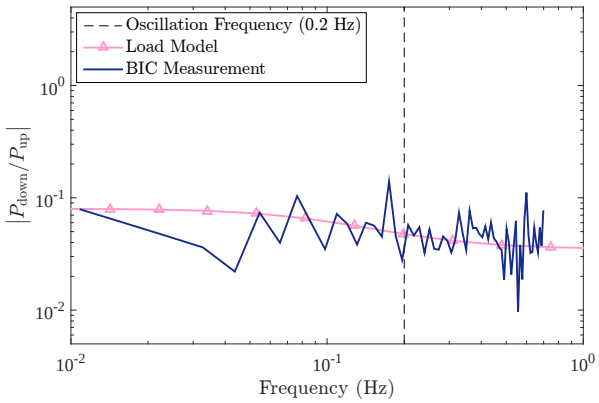

Figure 5: Power spectrum (in the frequency domain) of the amplitude ratio $|P_{\mathrm{down}}/P_{\mathrm{up}}|$ downstream and upstream of the valve from intermediate pressure (11.8 bar) measurements on the BIC prototype. Also showing the fitted load model according to Eq. 7.

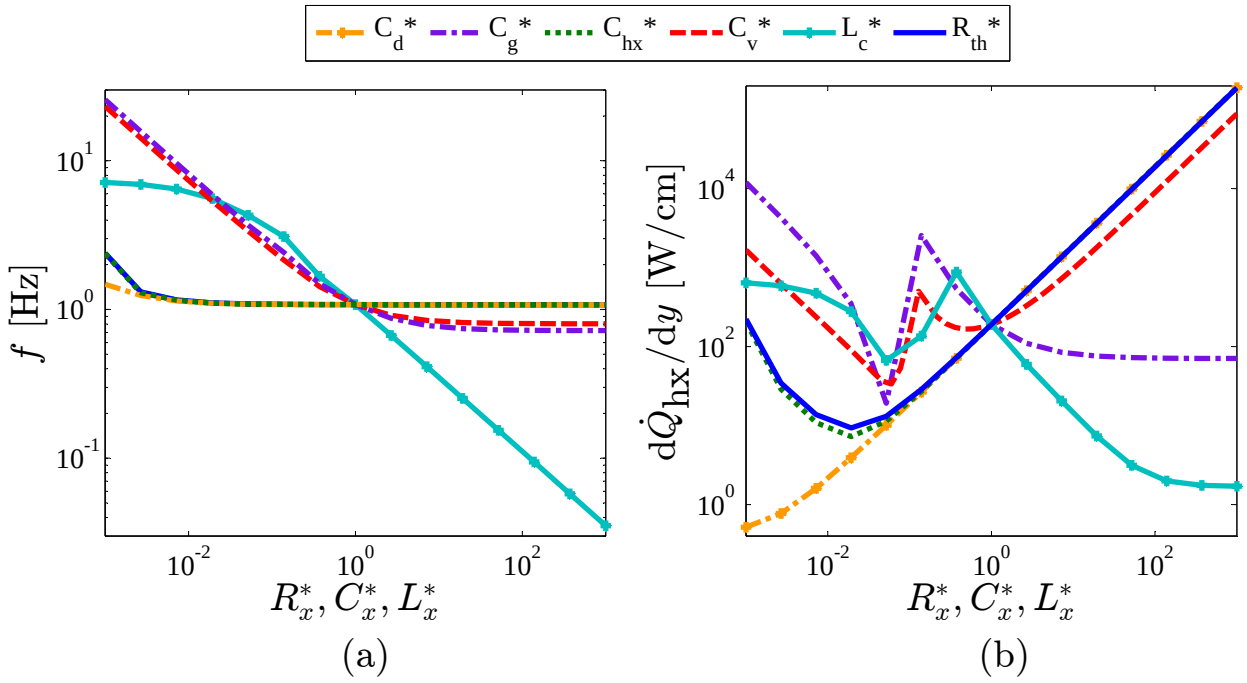

Figure 6: Variations in the: (a) oscillation frequency f; and (b) heat input rate gradient $\mathrm{d}\dot{Q}_{\mathrm{hx}}/\mathrm{d}y$ in the load-free engine at a mean pressure of 3.6 bar according to the DHX model as functions of the normalized parameters listed in the legend. Parameters not presented here have low or negligible influence on the frequency or heat input gradient.

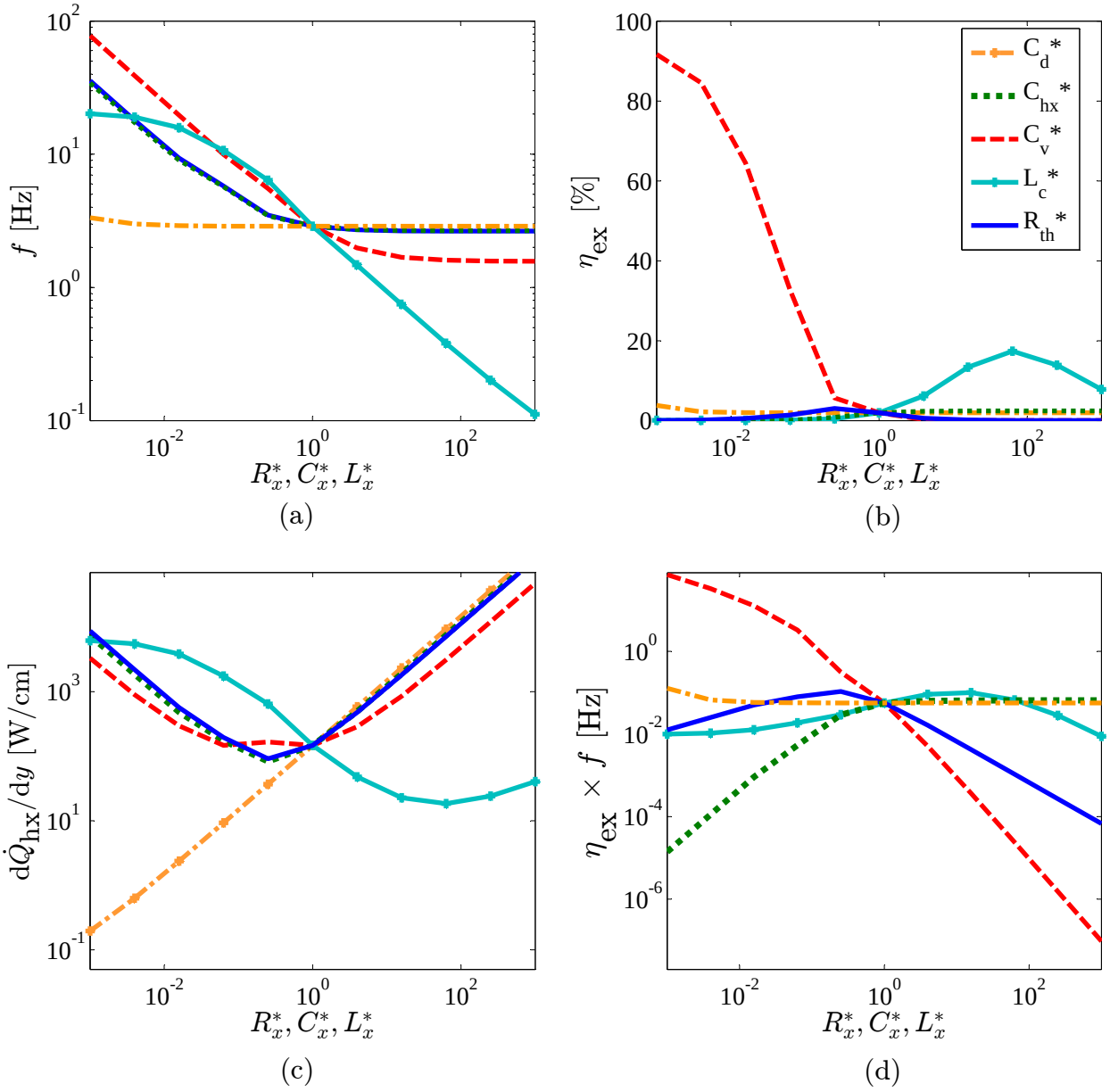

Figure 7: Variations in the: (a) the oscillation frequency f; (b) the exergy efficiency η_{ex}; (c) the heat-input rate gradient $d\dot{Q}/dy$; and (d) product of exergy efficiency and frequency $\eta_{ex} \times f$ (proportional to power output per unit heat input) in the loaded engine with a mean pressure of 18.1 bar as functions of the normalized parameters listed in the legend.

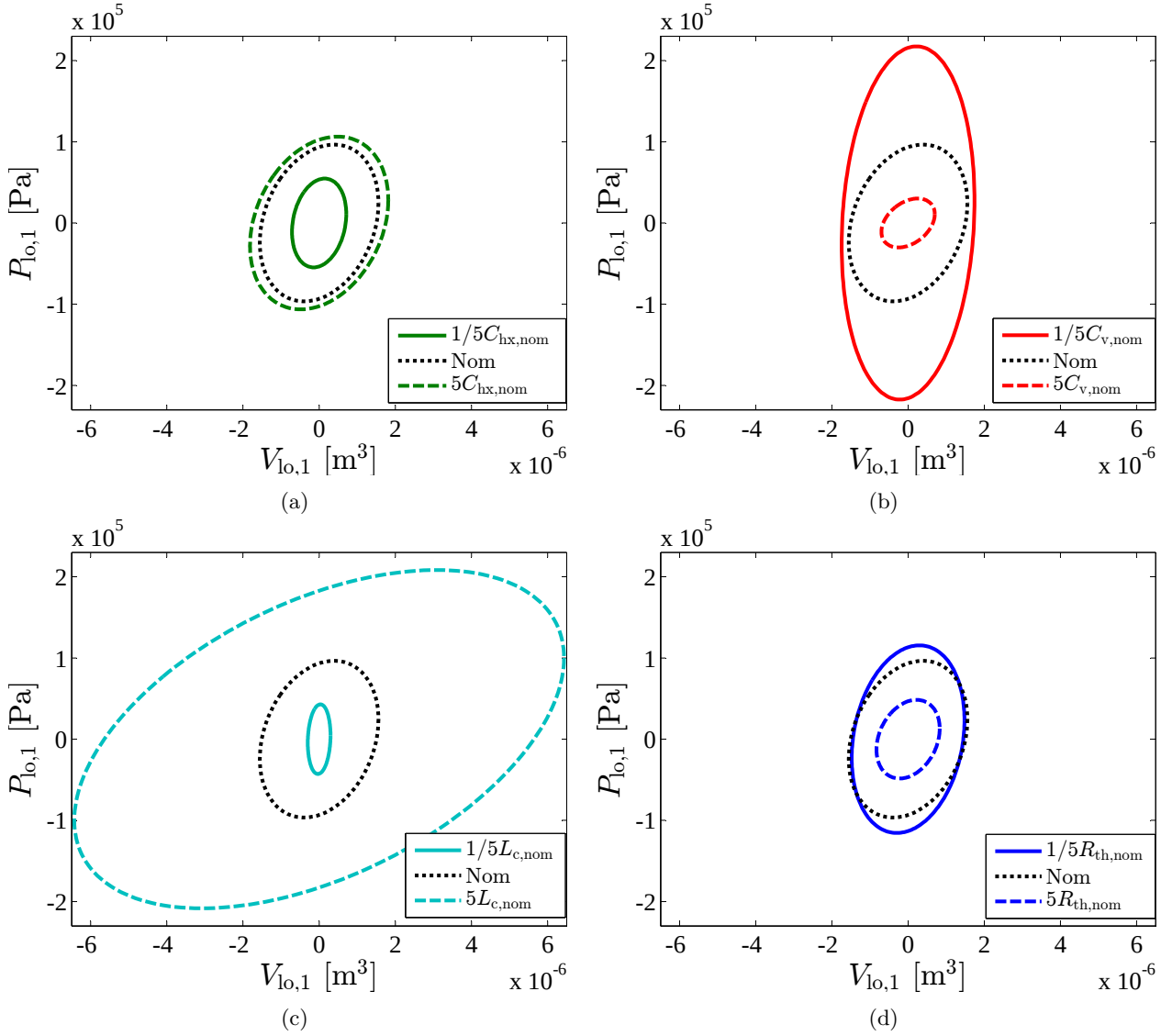

Figure 8: Linearized pressure-volume diagrams relating pressure $P_{\mathrm{lo},1}$ to the volume displacement $V_{\mathrm{lo},1}$ in the load for 5 times (dashed lines) and one fifth (solid lines) of nominal values of: (a) C_{hx}; (b) C_{v}; (c) L_{c}; and (d) R_{th}. The dotted line represents the nominal case. The area enclosed by the Lissajous curves represents the work output per oscillation. For all cases, the time-averaged pressure is 18.1 bar, and the exergy input rate into the engine is constant.

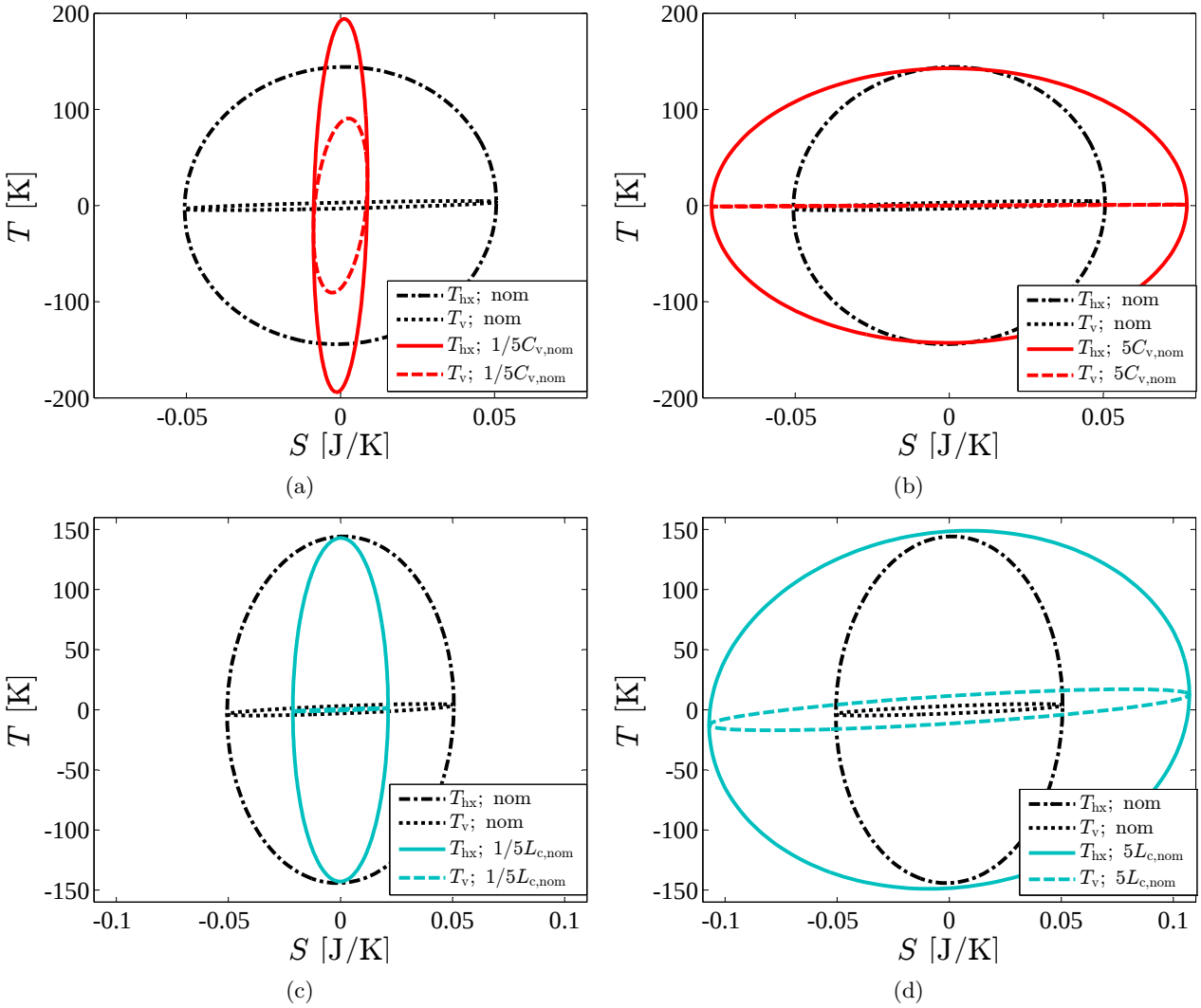

Figure 9: Linearized T–S cycle diagrams for 5 times and one fifth of nominal values of C_v ((a) and (b)); and L_c ((c) and (d)). The areas enclosed by the solid and dash-dotted lines (T_hx) represent the net exergy made available to the device in one oscillation; the dashed lines and dotted lines (T_v) represent the net exergy gained by the working fluid in one oscillation. The difference between both cycles amounts to the exergy destruction due to irreversible heat transfer between the heat exchangers and the working fluid. The temperature values on the vertical axes are not absolute temperatures but temperature differences to the respective equilibrium temperatures.

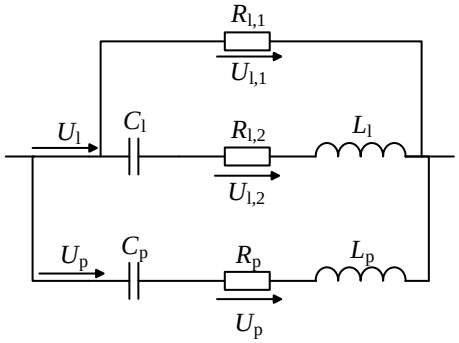

Figure 10: Circuit of piston and leakage model without slide bearing.